U.PORTO

FEUP FACULDADE DE ENGENHARIA
UNIVERSIDADE DO PORTO

MODELLING OF THE DYNAMIC BEHAVIOUR OF BALLAST ON RAILWAY BRIDGES

JOSÉ MARIA CORREIA DE OLIVEIRA BRANDÃO DE MENEZES

Dissertação submetida para satisfação parcial dos requisitos do grau de

MESTRE EM ENGENHARIA CIVIL — ESPECIALIZAÇÃO EM ESTRUTURAS E GEOTECNIA

Orientador: Pedro Aires Moreira Montenegro e Almeida

Coorientador: Matthias Baeßler

Coorientador: Patrick Simon

OUTUBRO DE 2024

MESTRADO EM ENGENHARIA CIVIL 2023/2024

DEPARTAMENTO DE ENGENHARIA CIVIL

Tel. +351-22-508 1901

✉ m.ec@fe.up.pt

Editado por

FACULDADE DE ENGENHARIA DA UNIVERSIDADE DO PORTO

Rua Dr. Roberto Frias

4200-465 PORTO

Portugal

Tel. +351-22-508 1400

✉ feup@fe.up.pt

http://www.fe.up.pt

Modelling of the dynamic behaviour of ballast on railway bridges

José Maria Menezes

Masters in Civil Engineering- Specialization in Structures and Geotechnics

October 15, 2024

Resumo

O principal objetivo desta dissertação é aprimorar o critério de limite de aceleração no tabuleiro atualmente utilizado para o projeto de pontes ferroviárias de alta velocidade. Atenção especial é dada ao comportamento do balastro quando sujeito a vibrações verticais, e entender o seu impacto na segurança operacional do comboio. Especificamente, como as acelerações verticais do tabuleiro da ponte afetam a estabilidade lateral do balastro e, portanto, o suporte da via. Seguindo a experiência adquirida com as linhas de alta velocidade francesas há mais de 30 anos, foi definido um valor limite de acelerações de 0,35g para pontes com vias balastradas, designado pelo comitê de especialistas ERRID214, e adotado na norma europeia EN1990-2 como o principal critério para controlar este fenômeno. Para alcançar este limite, vários testes experimentais foram realizados no passado sobre este tema, mas ainda existem vários pontos em aberto em relação à aceleração máxima que um tabuleiro de ponte ferroviária pode suportar sem afetar a estabilidade do balastro e, consequentemente, a segurança da via ferroviária. Portanto, para estudar mais a fundo este tópico, uma tarefa específica do Projeto Europeu InBridge4EU, na qual esta tese está integrada, foi estabelecida para ser realizada pela FEUP e BAM.

Experiencias e estudos anteriores mostraram que dois parâmetros predominantes na degradação da resistência lateral (também conhecida como "vibration-induced creep" do balastro) são a amplitude da aceleração e o número de ciclos aplicados à via balastrada. O estudo atual examina o impacto de passagens individuais de comboios na degradação da resistência devido à vibração. Para avaliar explicitamente o fenômeno da instabilidade do balastro com base em testes experimentais realizados no passado pela BAM, foram realizadas análises dinâmicas para obter respostas em aceleração que posteriormente serviram de input à metodologia de análise de instabilização.

Uma vez concluída a modelação da ponte através do software ANSYS, onde análises modais foram efetuadas para obter os modos de vibração da estrutura e respectivas frequências, procederam-se às análises dinâmicas para a passagem de vários comboios HSLM-A ("High Speed Load Model A"). Essas análises permitiram estudar os efeitos de ressonância desencadeados por cargas dinâmicas que amplificam a resposta da ponte. Posteriormente, com um código em MATLAB, implementado com os resultados obtidos no ANSYS, através da superposição modal e integração por passos temporais, foi possível calcular com precisão as acelerações verticais do tabuleiro. Além disso, métodos de análise de fadiga (contagem de ciclos pela técnica rainflow e acumulação de danos via a regra de Palmgren-Miner) foram utilizados para relacionar o impacto de uma única passagem do comboio com os resultados de testes e simulações em vias balastradas excitadas dinâmicamente sobre pontes.

Finalmente, com a integração dos resultados experimentais anteriores da BAM e o resultado deste estudo, foi possível obter uma compreensão mais abrangente do critério de aceleração. Isso permite um entendimento muito mais rigoroso dos efeitos a longo prazo sobre o balastro da ponte, particularmente o número de passagens de um determinado comboio que acumulam um deslocamento lateral via "vibration induced-creep". Através deste método, o critério de limite de aceleração excessivamente conservador pode ser aliviado ao examinar a influência que comboios es-

pecíficos têm em pontes específicas sobre a instabilidade do balastro. Esta é uma grande melhoria para o projeto e reavaliação de pontes ferroviárias sujeitas à excitação dinâmica.

Abstract

The main aim of this dissertation is to enhance the acceleration limit criterion currently used for the design of high speed railway bridges. Particular attention is given to the ballast behaviour when subjected to several types of vibrations, including harmonic and individual pulses, and understand its impact on the train's running safety. Specifically, how vertical bridge deck accelerations affect the lateral stability of the ballast and therefore the support of the track.

Following the experience gained from French high-speed lines more than 30 years ago, a threshold value for accelerations of 0.35g for bridges with ballasted tracks was defined, commissioned by the experts committee ERRID214, and adopted in the European norm EN1990-2 as the main criteria to control this phenomenon. To achieve this limit, several experimental tests were made in the past regarding this topic, but there are still several open points with respect to the maximum acceleration that a railway bridge deck can sustain without affecting the ballast's stability and, consequently, the train's safety. Therefore, to further study this topic, a specific task from the European Project InBridge4EU, in which this thesis is integrated, has been set to be carried out by FEUP and BAM.

Previous experiments and studies showed that two governing parameters in the degradation of lateral resistance (also known as "vibration-induced creep" of the ballast) are the acceleration amplitude and the number of cycles applied to the ballasted track. The current study examines the impact of single train passages on the vibration-induced creep. In order to explicitly assess the ballast instability phenomenon based on experimental tests performed in the past by BAM, modal analyses were conducted using the finite element software ANSYS.

Once the modelling was complete, dynamic analyses were performed for the passage of various HSLM-A trains ("High Speed Load Model A"). These analyses allowed studying resonance effects triggered by dynamic loads that amplify the bridge's response. Subsequently, with a numerical model in MATLAB, implemented with the obtained results from ANSYS, through modal superposition and time step integration it was possible to precisely predict the vertical deck accelerations. Furthermore, methods of fatigue analysis (rainflow counting and damage accumulation via the Palmer-Mingren rule) were used to relate the impact of a single train passage to the results from tests and simulations on harmonically excited ballasted track on bridges.

Finally, with the integration of previous experimental results by BAM and the outcome of this study a more comprehensive understanding of the acceleration criteria is possible. This enables a much more rigorous understanding on the long-term effects on the bridge's ballast, particularly the number of passages with a given train that accumulate to a lateral displacement via vibration-induced creep. Through this method, the overly conservative acceleration limit criterion can be alleviated by examining the influence specific trains on specific bridges have on ballast instability. This is major improvement for the design and reassessment of railway bridges subjected to dynamic excitation.

Acknowledgements

The completion of this work has been made possible through the contributions of several individuals, to whom I express my deepest gratitude:

To my advisor, Professor Pedro Aires Moreira Montenegro e Almeida, who was the main reason I had the opportunity to undertake this project at BAM in Berlin. For all his guidance and constant availability throughout the thesis, always demonstrating great professionalism and kindness;

To my co-advisors, Patrick Simon and Matthias Baeßler, for welcoming me so warmly at BAM and for their availability and assistance throughout all stages of the dissertation, imparting essential knowledge for its successful completion;

To my colleagues Carlos and Tomas, I thank them for their friendship and excellent company over the years.

To my entire family, especially my parents and siblings, for their encouragement and support throughout my life.

This thesis was developed within the project InBridge4EU, which received funding from Europe's Rail Joint Undertaking under the Horizon Europe research and innovation programme under grant agreement No. 101121 (Horizon-ER-JU-2022-EXPIR-02).

José Maria Menezes

"Everything we hear is an opinion, not a fact.
Everything we see is a perspective, not the truth."

Marcus Aurelius

Contents

List of Figures

List of Tables

List of Abbreviations

BAM	Bundesanstalt für Materialforschung und -prüfung
CWR	Continuous Welded Rail
EGD	European Green Deal
ERRI	European Rail Research Institute
EYR	European Year of Rail
FRA	Federal Railroad Administration
HSLM	High-Speed Load Model
LM71	Load Model 71
lin-lin	Linear-Linear
lin-log	Linear-Logarithmic
log-log	Logarithmic-Logarithmic
SNCF	Société Nationale des Chemin de Fer
TEN-T	Trans-European Transport Network

Chapter 1

Introduction

The railway system has significantly impacted global social and economic development in recent decades. In Europe, rail transport has been vital for achieving sustainable and competitive economic growth, especially through the high-speed rail network. High-speed rail is seen as the future of passenger transport, effectively meeting demands for mobility and comfort, contributing to sustainability, and adapting seamlessly to the changing energy paradigm. This is due to the fact that rail transport is cost-effective, environmentally friendly, fast, and has a high capacity for both passengers and freight. As a result, there is increasing interest in research in this area, which is driving the development of safer and more efficient vehicles to meet various challenges.

1.1 Scope

The European Union designated 2021 as the European Year of Rail (EYR) to promote the use of rail transport (European Parliament and Council of the European Union, 2020). The primary goal of this initiative was to demonstrate that rail transport is accessible, comfortable, and safe, with the lowest incidence of fatal accidents among land transport modes, as shown in Figure 1.1.

Figure 1.1: Number of fatal accidents by each type of transport (European Comission, 2021)

This decision is directly influenced by the European Green Deal (EGD) (Commission to the European Parliament et al., 2019), which is a plan for sustainable action within the European

Union concerning environmental and climate issues. The European Green Deal main goal is to ensure zero emissions by 2050, making Europe the first climate-neutral continent in the world. Figure 1.2 illustrates several aspects of the EGD.

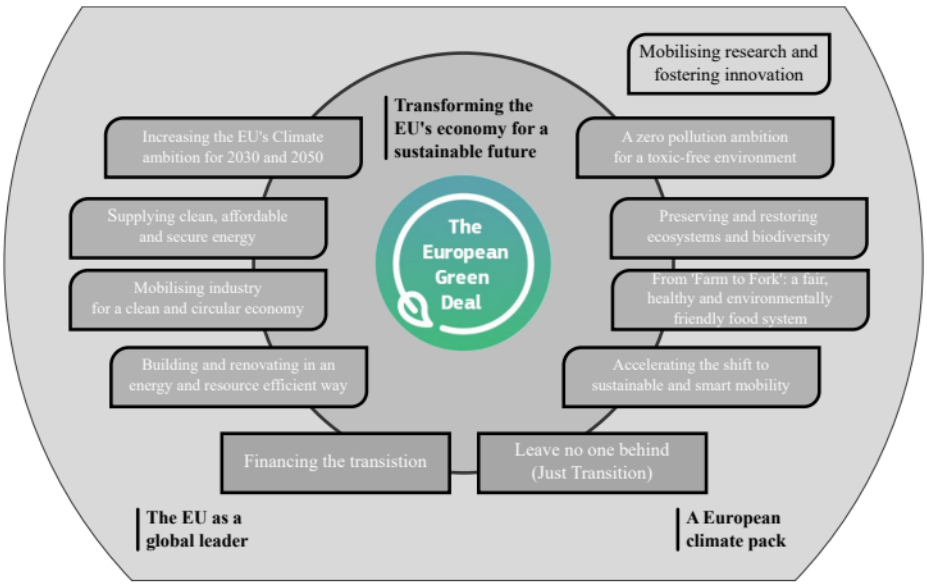

Figure 1.2: The European Green Deal (adapted from Commission to the European Parliament et al. (2019))

The EGD states that the transportation sector is responsible for a quarter of greenhouse gas emissions in the EU, and sets a goal of reducing that share by 90% by the year 2040. Figure 1.3 illustrates the distribution of greenhouse gas emissions across various modes of transport, indicating that road transport is the primary contributor, whereas rail transport has a minimal contribution of only 0.4

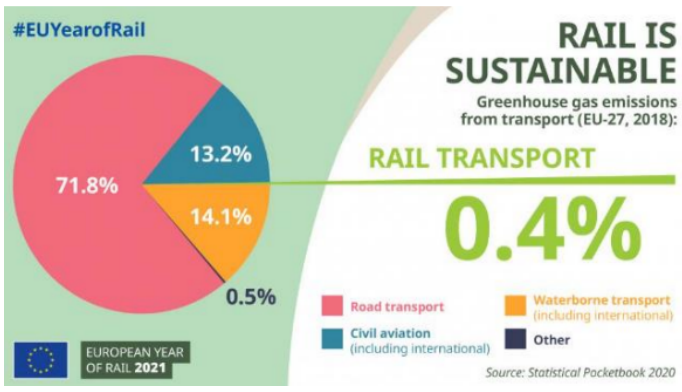

Figure 1.3: Distribution of greenhouse gas emissions by each type of transport (European Comission, 2021)

Furthermore, the EGD aims to shift a significant portion of inland freight from roads- which currently handle 75% of all freight transportation- to railways and inland waterways. Specifically, 50% of passenger and freight traffic over 300 km from road to rail by 2050 (30% of freight by

2030), achieving a 60% reduction in greenhouse gas emissions from the transport sector, completing the core TEN-T (Trans-European Transport Network) (see Figure 1.4) by 2030, and finishing the comprehensive TEN-T with rail connections to all main network airports by 2050. The strategies outlined by the European Commission for sustainable and smart mobility are therefore primarily based on doubling rail freight transport by 2050 and tripling high-speed rail passenger transport by 2050, both referenced to 2015 levels (European Commission, 2011). Thus, given the ambitious goals set by the European Commission (2021), a significant expansion of railway line capacity has already started and will be crucial in the coming years.

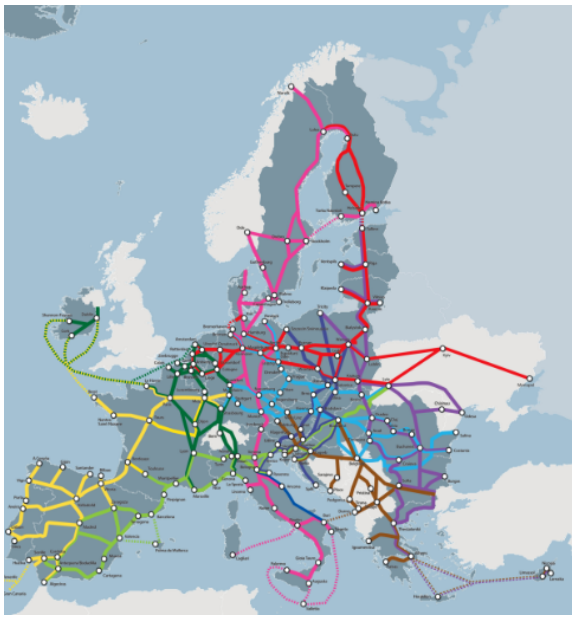

Figure 1.4: Trans-European Transport Network (TEN-T) Map (European Comission, 2021)

Expanding high-speed rail lines is particularly crucial due to the factor of travel time. Rail transport excels for journeys lasting up to 2.5 hours, whereas aviation becomes more dominant for trips exceeding 5 hours (International Union of Railways, 2018). As a result, the intermediate travel time range is a competitive area for both modes of transport. To enable rail to effectively compete in this middle range, it will be necessary to increase the capacity of railway infrastructure, including both conventional lines for passengers and freight as well as high-speed lines that provide rapid connections between cities within each country. With the rapid expansion of high-speed rail networks globally, there is an increasing need for numerous bridges and viaducts. This necessity arises primarily because high-speed rail lines require large curvature radii to ensure both safety and operational efficiency. Trains traveling at speeds up to 350 km/h require wider curves to manage the higher speeds and reduce lateral forces that could affect stability and passenger comfort. Sharp turns would otherwise lead to excessive centrifugal forces that can lead to the derailment of the trains. By using larger curvature radii, the impact of these forces is minimized, ensuring smoother and safer travel. It is crucial to ensure the track safety in order to maintain the integrity and reliability of high-speed rail systems.

Special attention is required for assessing railway safety in accordance with the European standards EN 1990 Annex A2 (2001) and EN 1991-2 (2017). These standards were developed based on studies by ERRI (1999) following issues observed on the first European high-speed line between Paris and Lyon (1981), particularly with small-span bridges. Problems such as resonance, ballast degradation, and rapid track deterioration were identified. As a result, the D214 ERRI committee established that for speeds over 200 km/h — where resonance effects are more likely—European standards now require dynamic analyses to evaluate the behavior of bridges. Static analyses alone do not address the dynamic amplification factors associated with these conditions. To address these dynamic effects, a specific acceleration limit criterion has been established as a key measure to ensure the stability of ballasted tracks and the safety of railway operations.

1.2 Objectives

The primary objective of this dissertation is to evaluate the current normative safety criterion for railway bridges, which is based on the vertical acceleration of the bridge deck, and to compare it with a direct approach that assesses ballast lateral stability through moving load analyses. Therefore, the main aim is to delve deeper into the factors contributing to ballast instability as they relate to a established criterion, based on experimental results, and to develop a series of curves that relate different acceleration amplitudes to ballast instability. The vertical acceleration of the deck is a criterion based on the assumption that when the bridge reaches accelerations of 0.7g, can lead to a loosening of the ballast fabric posing a potential risk of lateral track instability and consequent risk of derailment. The limit of 3.5 m/s² is derived from applying a safety factor of 2.0 to the previously mentioned value.

The dynamic analysis focuses on evaluating the structure's behavior in terms of accelerations due to high-speed train loads and determining the accumulated damage from single train passages for all HSLM-A load models.

For this dynamic analysis, ANSYS is used to model the structures and the vehicle with finite elements, while MATLAB is employed to simulate the train crossing the bridge at resonant speeds, providing the necessary results for the damage evaluation.

1.3 Outline of the Research Thesis Project

This research thesis project is divided into 5 chapters, including this introduction. Chapter 2 is a review of methodologies utilized to assess the dynamic behaviour of high-speed railway bridges, including design considerations and aspects concerning the modelling and solving of the bridge-train dynamic systems. Additionally, Chapter 2 explores the mechanisms behind ballast instability, offering insights into how these factors impact the stability of ballasted tracks. Chapter 3 describes the approach used to evaluate the dynamic behavior of railway bridges, including the use of ANSYS and MATLAB for finite element modeling and simulation of train passages at different resonant speeds. Additionally, it details how the accumulated damage from single train

passages will be assessed using past BAM experience data. Chapter 4 describes the bridges studied in this work, as well as the high-speed trains. The bridge numerical model developed in ANSYS is presented, as well as the results from the dynamic analysis conducted in MATLAB. From the results of these analyses, the mid-span bridge accelerations and the accumulated damage to the ballast layer from each individual train passage are presented. Given this approach, the influence of specific trains on ballast instability on specific bridges is examined. Finally, in Chapter 5, the conclusions of the obtained results are presented, along with proposals for future work related to the topic.

Chapter 2

Literature Review

2.1 Introduction

In this chapter, the main regulatory aspects for the design of railway bridges are presented according to EN1991-2 (2017) (section 2.2). A normative approach for safety checks is presented according to EN1990-Annex A2 (2001) and EN1991-2 (2017) (section 2.3). A more in-depth analysis of the research related to the deck acceleration limit and the vibration-induced creep phenomenon are presented (sections 2.4 and 2.5). Finally, the methods for analyzing the dynamic behavior of the bridge and train are shown (section 2.6).

2.2 Design Considerations Regarding Dynamic Effects on High-Speed Railway Bridges

2.2.1 Static analysis

The static effects resulting from different traffic actions, from unloaded trains to heavy traffic, are defined in EN1991-2 through four distinct load models: Load Model 71 (LM71), the Load Models SW/0 and SW/2, the High-Speed Load Model (HSLM) and the model related to the unloaded train. The static effects are especially related to the design considerations of railway bridges. Subsequently a more detailed insight from the mentioned load models will be presented.

2.2.1.1 Load Model LM71

The LM71 represents the static effect of vertical loading due to normal rail traffic, and it consists, of four concentrated loads (Q_{vk}) of 250 kN each and uniformly distributed loads (q_{vk}) of 80 kN/m, as illustrated in Figure 2.1. These values should be multiplied by a classifying factor α, in case of railway traffic that is either heavier or lighter than the normal traffic. Under conditions of lighter traffic, the factor α can assume values of 0,75, 0,83 or 0,91, while for heavy traffic, it can be taken as 1,10, 1,21, 1,33 or 1,46.

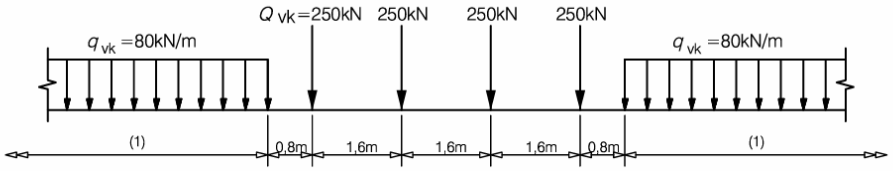

Figure 2.1: Load Model LM71 (EN1991-2, 2003)

2.2.1.2 Load Models SW/0 and SW/2

The SW/0 Load Model represents the static effect of vertical loading due to normal railway traffic on continuous bridges, while the SW/2 Load Model represents the static effect of vertical loading due to heavy railway traffic on continuous bridges. The illustrated load arrangement in Figure 2.2, should be considered with the values of the vertical loads provided in Table 2.1.

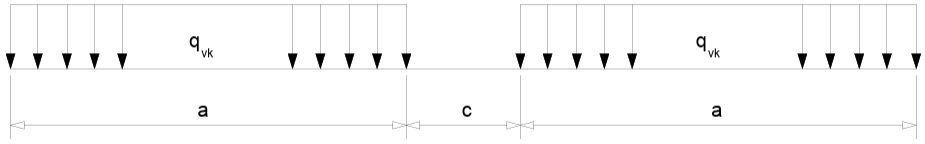

Figure 2.2: Load Models SW/0 and SW/2 ((EN1991-2).

Load Model	qvk [kN/m]	a [m]	c [m]
SW/0	133	15,0	5,3
SW/2	150	25,0	7,0

Table 2.1: Characteristic values for vertical loads for Load Models SW/0 and SW/2 (adapted from, EN 1991-2, 2017)

Additionally, if the SW/0 load model aligns with the conditions outlined in 2.2.1., it should be multiplied by the factor α.

2.2.1.3 Load Model "unloaded train"

The unloaded train model consist of a uniformly distributed vertical load with a characteristic value of 10 kN/m, used to verify the lateral and vertical stability of bridges when subjected to lateral and vertical actions.

2.2.1.4 Dynamic effects

Furthermore, the EN 1991-2 (2017) considers the dynamic effects induced by the moving traffic, defining the dynamic amplification factor Φ. This involves multiplying the static effects generated by Load Models LM71, SW/0, and SW/2 by the dynamic amplification factor (Φ), in

order to simulate the dynamic effects. However, during the calculation of the Φ factor, resonance effects were not taken into account.

Depending on the track maintenance level, this factor can either have the value of Φ_2 for tracks with careful maintenance or Φ_3 if the track has standard maintenance. The dynamic coefficients Φ_2 and Φ_3 are calculated using Equations 2.1 and 2.2, respectively ($L_\Phi(m)$ represents the determinant length).

$$\Phi_2 = \frac{1.44}{\sqrt{L_\Phi} - 0.2} + 0.82 \qquad (1.00 \leq \Phi_2 \leq 1.67) \tag{2.1}$$

$$\Phi_3 = \frac{2.16}{\sqrt{L_\Phi} - 0.2} + 0.73 \qquad (1.00 \leq \Phi_3 \leq 2.0) \tag{2.2}$$

In case of a static analysis with the passage of real trains or the HSLM, it is essential to consider a dynamic amplification factor 1 + φ, which is determined by the following expression:

$$1 + \varphi = 1 + \varphi' + \lambda\, \varphi'' \tag{2.3}$$

where φ' represents the dynamic amplification due to traffic, φ'' is the component corresponding to track and wheel irregularities of the vehicles and λ a factor related to the track conditions, considered 1.0 for tracks with normal maintenance levels and 0.5 for tracks with careful maintenance levels.

The φ' is given by the following expression, where:

$$\varphi' = \begin{cases} \frac{K}{1-K+K^4}\ for K < 0,76 \\ 1,325\ \ for K \geq 0,76 \end{cases} \tag{2.4}$$

$$K = \frac{v}{2 L_\phi n_0} \tag{2.5}$$

with v being the maximum speed (m/s) and n_0 corresponding to the bridge's first natural bending frequency (Hz). Equation 2.6 shows the component representing track irregularities and wheel imperfections, φ'', with:

$$\varphi'' = \frac{\alpha}{100}\left[56 e^{-\left(\frac{L_\phi}{10}\right)^2} + 50\left(\frac{L_\phi n_0}{80} - 1\right) e^{-\left(\frac{L_\phi}{20}\right)^2}\right] \geq 0 \tag{2.6}$$

$$\alpha = \begin{cases} \frac{v}{22}\ se\ v \leq 22 m/s \\ 1\ se\ v > 22 m/s \end{cases} \tag{2.7}$$

As mentioned, all these factors are only applicable for non-resonant effects, particularly in situations involving low-speed train traffic. However, with the introduction of high-speed rail, circulation speeds have reached and surpassed 200 km/h, presenting challenges not previously

encountered, such as resonance effects. In order to determine whether a dynamic analysis is required, the EN1991-2 presents a flowchart, displayed in Figure 2.3.

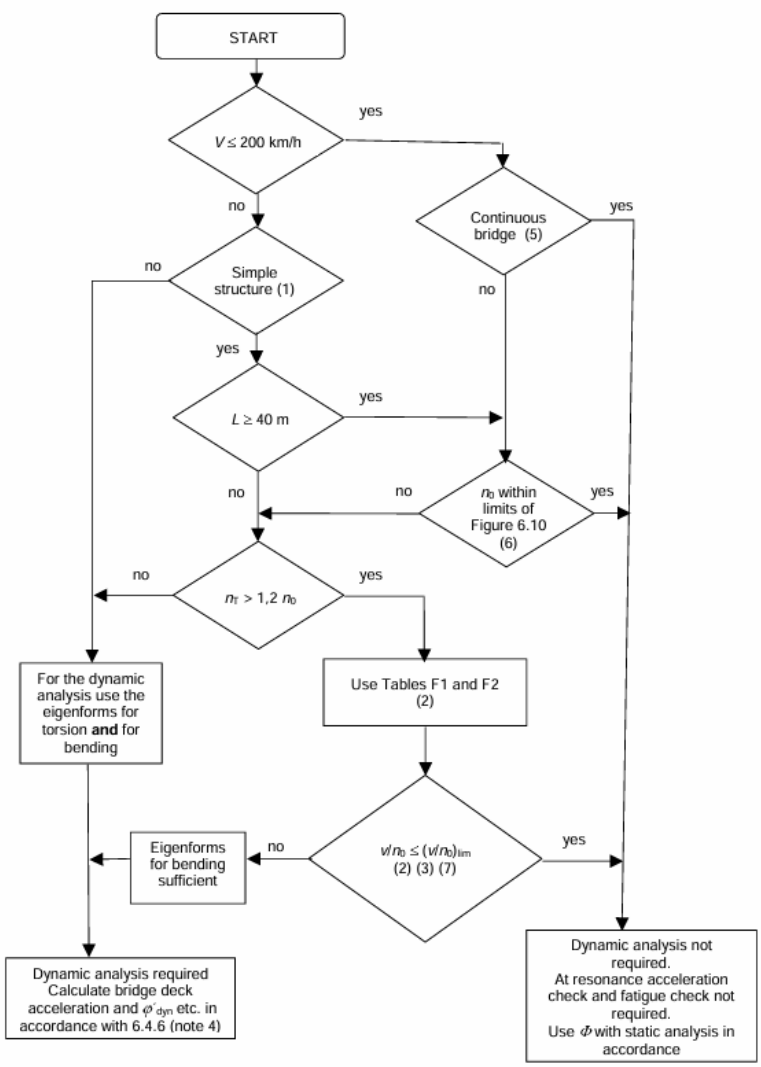

Figure 2.3: Flow chart for determining whether a dynamic analysis is required (EN 1991-2, 2017)

Where V is the maximum line speed, L the span length of the bridge, n_0 the first natural frequency for bending and n_T the first natural frequency for torsion, v the maximum nominal speed and $(v/n_0)_{lim}$ is specified in Tables F1 and F2 of Annex F of EN 1991-2 (2017). Moreover, EN 1991-2 also establishes limits for the frequency of the first vertical mode n_0, within which a dynamic analysis is not required.

These limits are defined in Figure 2.4 in terms of the natural frequency of the structure (n_0), based on the span L.

The upper limit n_0^{sup}, represented by curve *1*, is associated with track irregularities and is defined by the following expression:

$$n_0 = 94,76L^{-0,748} \tag{2.8}$$

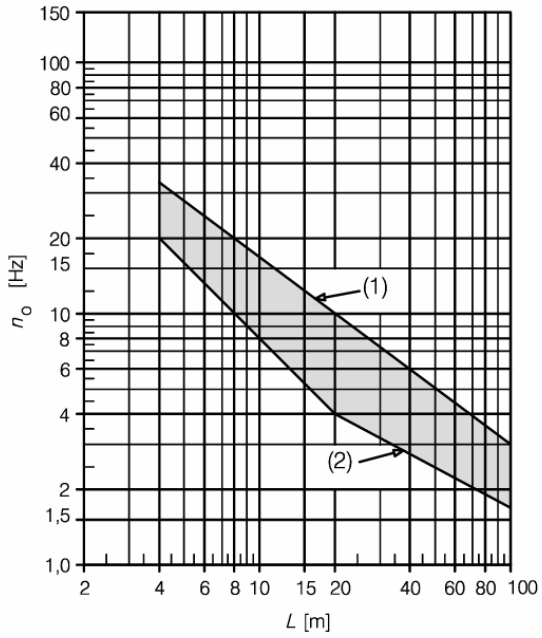

Key
(1) Upper limit of natural frequency
(2) Lower limit of natural frequency

Figure 2.4: Limits of bridge natural frequency n_0 [Hz] as function of L[m] (EN1991-2, 2017)

The lower limit $n_0^{\inf}$, represented by curve *2*, is associated with dynamic amplifications and is defined by:

$$n_0^{\inf} = \begin{cases} \dfrac{80}{L}, & 4m \leq L \leq 20m \\ 23,58L^{-0.592}, & 20m \leq L \leq 100m \end{cases} \tag{2.9}$$

2.2.2 Dynamic analysis requirements

2.2.2.1 Load Models

Dynamic analysis should be performed considering the characteristic axle load values of the specified real trains intended to operate on the structures where speeds exceeds 200 km/h. Additionally, the analysis shall also be conducted using Load Model HSLM in order to comply with the European high speed interoperability requirements. The ERRI D 214/RP 9, in Annex E, lists the real trains properties currently operating on the European high-speed rail network, classifying them as either articulated, conventional or regular, as depicted in Table 2.2.

Train	Type	N	L	P	d
ETR Y500	Conventional	48	295.7	120	26.1
Eurostar 373	Articulated	48	386.67	170	18.7
ICE2	Conventional	56	350.52	112	26.4
Talgo AV2	Regular	40	356.05	170	13.14
TGV Atlantique	Articulated	60	468.14	170	18.7
Thalys 2	Articulated	52	393.34	170	18.7
Virgin	Conventional	44	258.7	170	23.9

Table 2.2: Real trains' properties for moving load dynamic analysis (adapted from (adapted from (ERRI D214/RP 9, 1999)

N represents the number of axles, Lt (m) is the total length of the train, P (kN) the most frequent axle load and d (m) is the distance between regularly spaced axle groups.

Articulated trains are defined by two double-axle bogies shared between adjacent cars, conventional trains have two independent double-axle bogies per car, and regular trains have single-axle bogies shared by adjacent cars (see Figure 2.5)

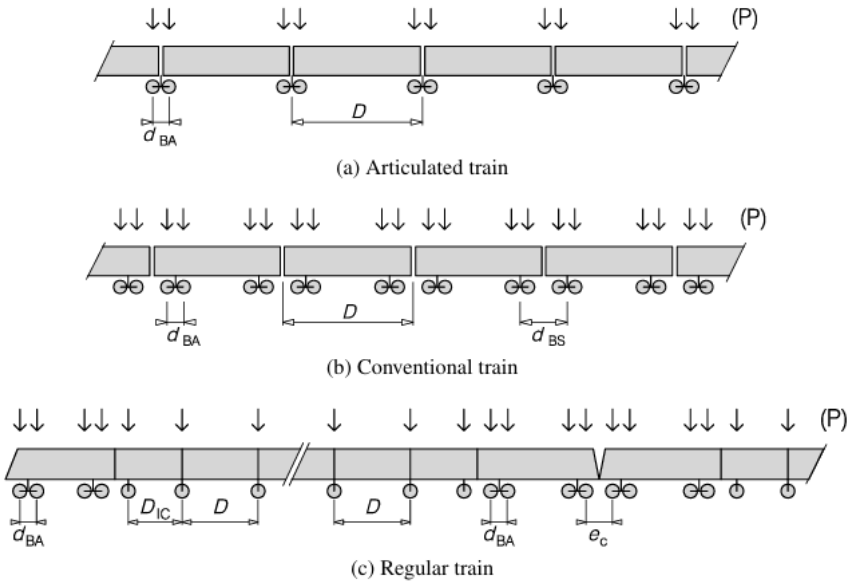

Figure 2.5: Train type configurations (adapted from EN1991-2, 2017)

The HSLM load model, consisting of the HSLM-A and HSLM-B load models, was specifically designed to ensure the interoperability concept, in order to account for all potential dynamic effects that may occur due to different trains circulating on the European high-speed rail network.

The HSLM-A consists of 10 trains, each composed of two cars, two end coaches, and N intermediate coaches, as depicted in Figure 2.6. The number of intermediate coaches (N), the coaches length (D), the bogie axle spacing (d), and the value of the Point forces (P) are indicated in Table 2.3.

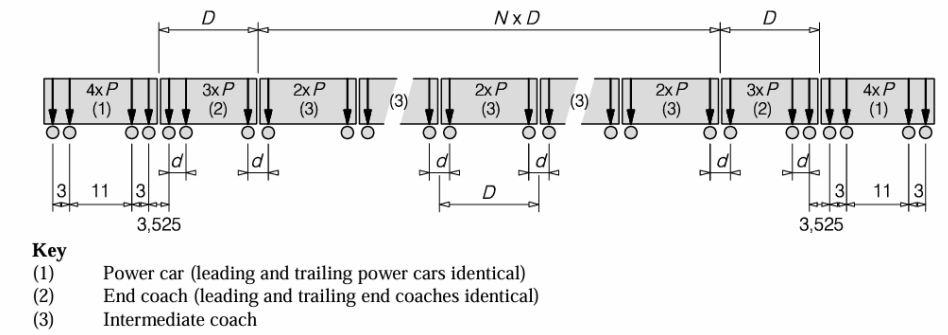

Figure 2.6: HSLM-A configuration (EN1991-2, 2017)

Universal Train	Number of intermediate coaches N	Coach length D [m]	Boogie axle spacing d [m]	Point force P [kN]
A1	18	18	2,0	170
A2	17	19	3,5	200
A3	16	20	2,0	180
A4	15	21	3,0	190
A5	14	22	2,0	170
A6	13	23	2,0	180
A7	13	24	2,0	190
A8	12	25	2,5	190
A9	11	26	2,0	210
A10	11	27	2,0	210

Table 2.3: HSLM-A' properties (adapted form EN1991-2, 2017)

The HSLM-B consists of N point loads of 170 kN uniformly spaced at a distance d, as shown in Figure 2.7. The values of N and d are defined in Figure 2.8 as a function of the span (L) of the bridge.

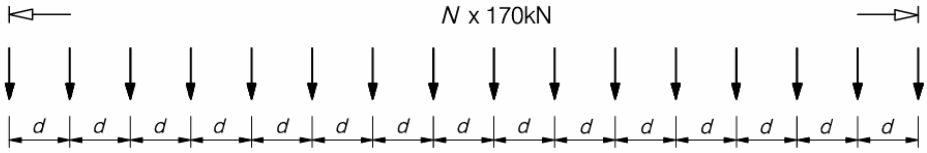

Figure 2.7: HSLM-B configuration (EN1991-2, 2017)

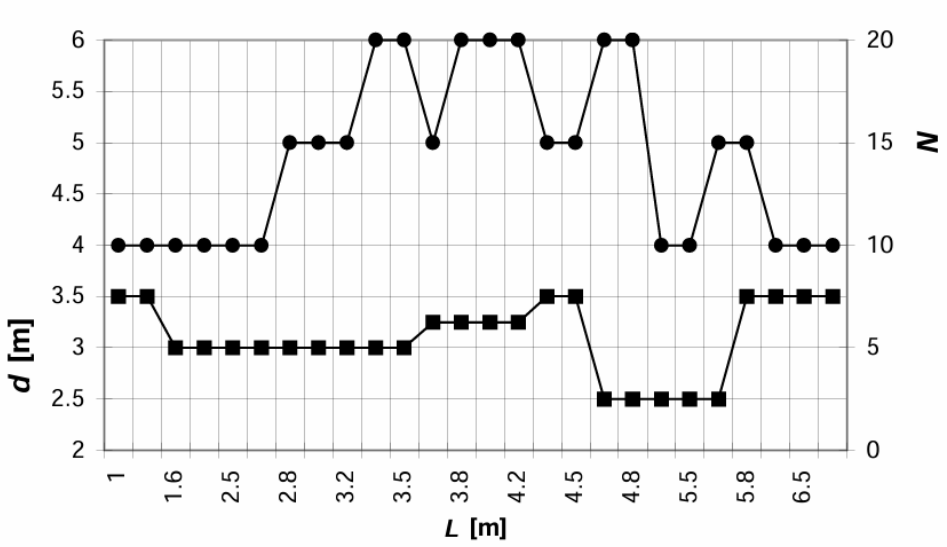

Figure 2.8: Parameters N and d as a function of L for HSLM-B (EN 1991-2, 2017)

The span of the bridge, L, along with it´s structural configuration, are crucial for defining which load model should be used in the dynamic analysis, whether it's HSLM-A or HSLM-B, as presented in Table 2.4.

Structural configuration	Span	
	L <7	L >7
Simply supported span	HSLM-B	HSLM-A
Continuous structure or Complex structure	HSLM-A Trains A1 to A10 inclusive	HSLM-A Trains A1 to A10 inclusive

Table 2.4: Application of HSLM-A and HSLM-B (adapted from EN1991-2, 2017)

2.2.2.2 Speeds to be considered

When conducting a dynamic analysis a range of velocities, for each Real Train and Load Model HSLM, should be considered. This range spans from an initial velocity of 40 m/s (144 km/h) to the maximum design speed v_{DS}, defined as 1.2 times the Maximum Line Speed at the site. At resonance velocities, the speed increment should be reduced to allow for a better identification of response peaks.

The resonant velocity for simple supported bridges that can me modelled as a line beam is definied as:

$$v_i = n_0 \cdot \lambda_i \tag{2.10}$$

with n_o being the first natural frequency of the unloaded structure and λ_i the principal wavelength of frequency of excitation, that may be estimated by:

$$\lambda_i = \frac{d}{i} \tag{2.11}$$

where d represents the regular spacing of groups of axles and i can take the values 1, 2, 3, or 4.

2.2.2.3 Bridge parameters

a) Stifness

The stiffness is essential for figuring out a structure´s natural frequency, but it is challenging to assess accurately because it depends on factors such as structural type, geometry, and materials used. Overestimating the bridge stiffness will result on a overestimation of the natural frequency of the structure and speed at which resonance occurs. To address this, a lower limit value of stiffness shall be used throughout the entire structure (ERRI D214/RP9, 1999).

b) Mass

Given the fact that the natural frequencies of the structure decreases as the mass of the structure increases, and that the dynamic load effects occur at resonant peaks when the frequency of loading is an integer multiple of the natural frequency of the structure, an overestimation of the mass leads to a decrease in resonance velocities. This scenario reflects a conservative evaluation of critical velocities, indicating a cautious anticipation that the structure might vibrate more easily than it actually does. On the other hand, given that the maximum acceleration at resonance is inversely proportional to the mass of the structure, an underestimation of the mass, leads to an increase in the magnitude of accelerations. Therefore, two distinct analysis shall be conducted: i) One with an estimate of the lower bound value of mass for predicting maximum deck accelerations; ii) another with an overestimation of the mass to predict the lowest velocities at which resonant effects are likely to occur.

c) Damping

Damping refers to the mechanical energy dissipated by the structure. This dissipation occurs due to the fundamental damping characteristics of both structural and non-structural materials, as they are interconnected, as well as the energy dissipated to the ground at support zones. A study conducted by the ERRI D214/RP9 (2001) concluded that the peak of a structure at resonance is highly dependant upon damping, with the dynamic response being inversely proportional to structural damping.

Experimental measurements of the overall damping coefficient across a series of different bridges with different spans and structural typologies (see Figure 2.9), concluded there is a correlation between span length and damping, with damping increasing as the span decreases. Based on this experiment the European Standard EN 1991-2 defines three curves to estimate the damping

of a bridge, depending on it´s span length and structural configuration. These curves represent the lower limits of the damping obtained in the measurements, aiming to provide conservative estimates of damping, as depicted in Table 2.5.

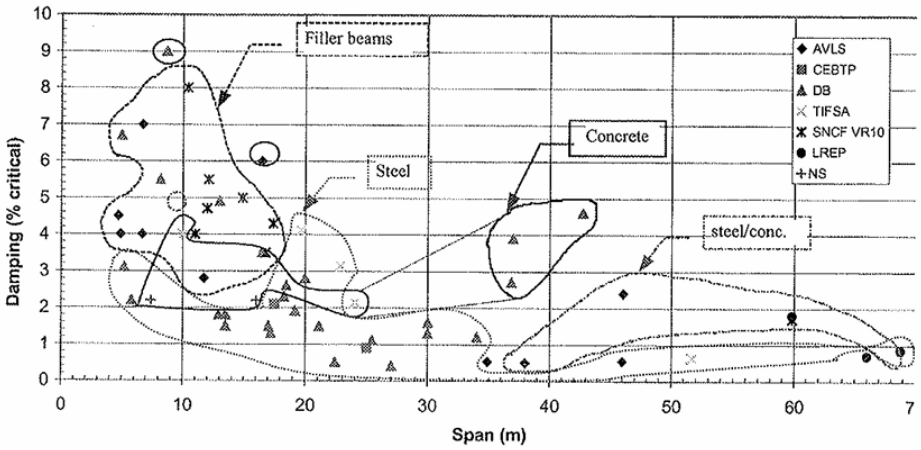

Figure 2.9: Damping as a function of span (Montenegro et al., 2021b)

Bridge type	ζ Lower limit of percentage of critical damping [%]	
	Span L <20m	Span L >= 20m
Steel and composite	ζ = 0,5 + 0,125 (20 - L)	ζ = 0,5
Prestressed concrete	ζ = 1,0 + 0,07 (20 - L)	ζ = 1,0
Filler beam and reinforced concrete	ζ= 1,5 + 0,07 (20 - L)	ζ = 1,5

Table 2.5: Values of damping to be assumed for design purposes (adapted from EN 1991-2, 2017)

2.3 Normative Criteria

2.3.1 Normative Criteria for Structural Safety

According to EN 1991 2 (2003), in the bridge design, considering all the effects of vertical traffic loads, the calculation values shall be determined by the most unfavorable of the following equations:

$$\left(1+\varphi'_{dyn}+\varphi''/2\right)\times\begin{pmatrix}HSLM\\ \text{or}\\ RT\end{pmatrix} \tag{2.12}$$

or

$$\Phi\times(LM71"+"SW/0) \tag{2.13}$$

where the HSLM refers to the load model for high speed lines, *RT* represents the loading due to all Real Trains, LM71 "+" SW/0 is Load Model 71 and Load Model SW/0 for continuous bridges,

both defined in the subsections 2.2.1.1 and 2.2.1.2, respectively. The dynamic enhancement φ'_{dyn} can be defined by the following expression

$$\varphi'_{dyn} = \max \left| y_{dyn}/y_{stat} \right| - 1 \tag{2.14}$$

with y_{dyn} being the the maximum dynamic response, at any specific point in the structure, due to a Real Train or Load Model HSLM and y_{stat} corresponding to the maximum static response of the structure. The factor φ'' is a amplification factor that takes into account track defects and vehicle imperfections and Φ is the dynamic factor.

2.3.2 Normative Criteria for Railway Traffic Safety

The limitations established in EN 1990 Annex A2 and EN 1991-2, aiming to ensure the safety of the track, relate to: vertical and transverse deformation of the bridge deck, deck twist, settlement of the vertical and horizontal support at the end of the bridge, vertical acceleration, and lateral vibration of the bridge deck

2.3.2.1 Vertical deformation of the bridge deck

In order to ensure an acceptable vertical track radius, the vertical deformation of the deck, denoted as δ_v (see Figure 2.10), is limited by the EN 1990-Annex A2 (2001) standard. According to this norm, the maximum total vertical deflection caused by the vertical traffic load models LM71 and SW/0 or SW/2 (EN 1991 2, 2017), cannot exceed $L/600$, where L is the span length. In case of large span bridges both the load model LM71 and SW/0 have to be considered in the design.

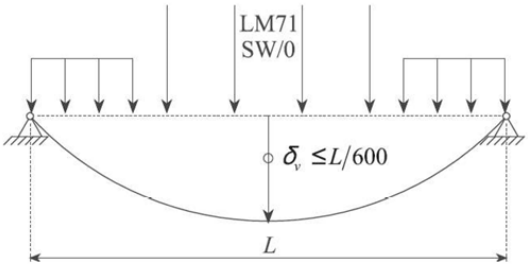

Figure 2.10: Vertical deflection of the deck (Montenegro et al., 2021b)

2.3.2.2 Desk twist

Regarding deck twist, the EN1990-Annex A2 aims to minimize the risk of train derailment, by limiting the maximum twist t for any given deck as shown in Figure 2.11. The twist of the deck is calculated considering the characteristic values of load model LM71 (or SW/0 or SW/2), affected by the dynamic and classifying factors and the High-Speed Load Model (HSLM) including centrifugal effects, as defined in EN 1991 2 (2017). Considering a track gauge of 1435 *mm* measured

over a length of 3 m, the maximum deck twist t should not exceed the values presented in Table 2.6.

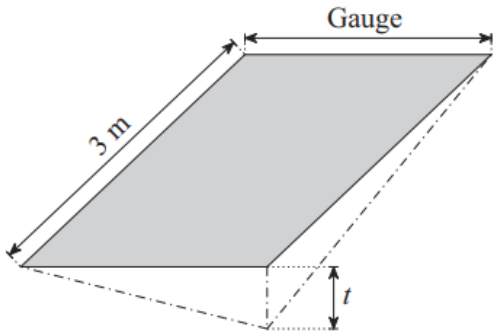

Figure 2.11: Definition of deck twist t (adapted from EN 1990-Annex A2 (2001))

Speed range V (km/h)	Maximum deck twist t (mm/3m)
$V \leq 120$	4,5
$120 \leq V \leq 200$	3,0
$V > 200$	1,5

Table 2.6: Design limits of deck twist (adapted from EN1990 Annex 2, 2001)

2.3.2.3 Transverse deformation of the bridge deck

Furthermore, the EN 1990-Annex A2 (2001) limits the transversal deflection of the deck δ_h (Table 2.7), to ensure that both the angular variation and the horizontal radius of curvature are satisfied. The angular variations can refer either to the transverse rotations at the end of the deck, θ_h, or the variation of transverse rotations between two adjacent spans, $\theta_{h1} + \theta_{h2}$, as illustrated in Figure 2.12. For the verification of this condition, the structure must be considered for characteristic combinations of: Load model LM71 and SW/0, as appropriate, multiplied by the dynamic factor. Additionally, wind loads, nosing and centrifugal forces and the effect of transverse differential temperature across the bridge, in accordance with EN 1991-2 (2017), must also be taken into account.

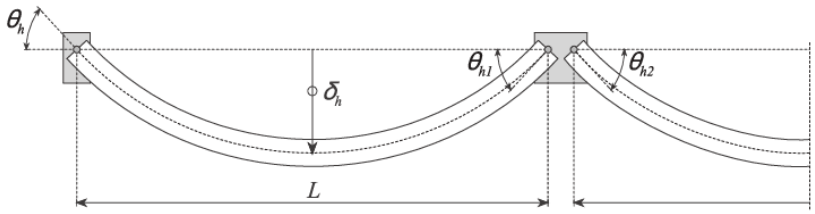

Figure 2.12: Transverse deflection (Montenegro et al., 2021b)

Speed V (km/h)	Maximum angular variation (rad)	Maximumu radius of curvature (m)	
		Single Span	Multi-Span
$V \leq 120$	0.0035	1700	3500
$120 \leq V \leq 200$	0.0020	6000	9500
$V > 200$	0.0015	14000	17500

Table 2.7: Maximum horizontal rotation and change of radius of curvature (adapted from EN1991-2, 2017)

2.3.2.4 Settlement of the vertical support at the end of the deck

EN1990-Annex A2 also limits the vertical and longitudinal displacements, of the upper surface, at the end of the deck. Implementing this requirement is crucial to avoid track instability, limit uplift forces on rail fastening systems and restrict additional rail stresses. Concerning the vertical displacement of the upper surface of the deck δ_v (see Figure 2.13), relative to adjacent construction (abutment or another deck) caused by factors such as LM71 (or SW/0), and due to unfavourable temperature variation, cannot exceed 3 *mm* or 2 *mm* in lines whose maximum allowed speed is up to 160 km/h or over 160 km/h, respectively.

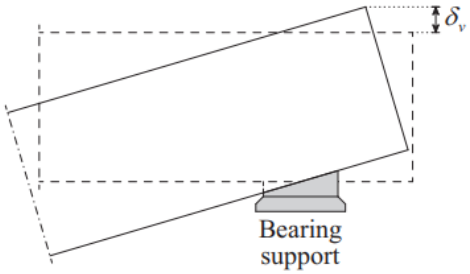

Figure 2.13: Vertical displacement of the upper surface of the deck δ_v (Montenegro et al., 2021)

2.3.2.5 Settlement of the horizontal support at the end of the deck

Regarding the longitudinal displacement of the upper deck surface at the deck's end, the restriction is crucial for minimizing disruptions to track ballast and the surrounding track structure. EN 1991-2 (2003) limits the longitudinal displacement, denoted as δ_h, relevant to the adjacent structure (abutment or another deck) due to traction and breaking, to 5 *mm* for continuously welded rails without expansion devices or 30 *mm* with expansion devices. The longitudinal displacement δ_h (see Figure 2.14), calculated taking into account the characteristic values of the vertical traffic load model LM71 (or SW/0, if applicable), is limited to 8 *mm* considering the combined behaviour of both structure and track, or 10 *mm* otherwise.

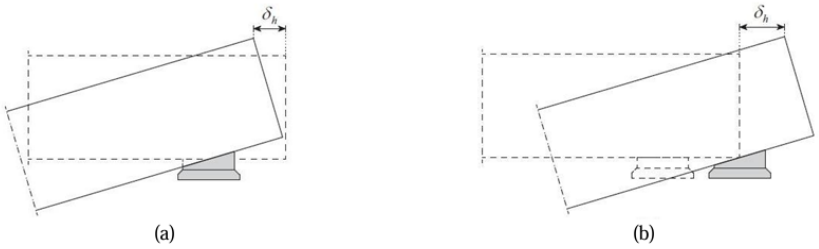

Figure 2.14: Longitudinal displacement of the upper surface of the deck (delta)h (a) fixed support and (b) guided support (Montenegro et al., 2021b)

2.4 Ballast stability degradation problem

2.4.1 Initial Considerations

Exploring ballasted tracks in greater detail, significant vibrations on the bridge deck can result in increased settlements, leading to high track irregularities. The vertical shaking of the track on bridge decks has been a major concern for years and led to some restrictions in acceleration limits. The main issue, regarding these vibrations is that it reduces the lateral resistance of the ballast, posing a potential risk of lateral track instability and consequent risk of derailment.

Vertical accelerations can lead to a loosening of the ballast fabric and following this, permanent vertical deformations of the sleeper occur. Acknowledging the fact that track deformation due to deterioration is mainly a maintenance problem, the main issue emerges with the lateral behaviour of the track, as a consequence of the bridge deck vibrations. Thus, large bridge-deck accelerations caused by rail traffic are limited to ensure the track secures its stability and integrity.

2.4.2 Research related on the deck acceleration limit

When high-speed trains were introduced in France on the Paris-Lyon line, resonance issues were identified by the SNCF (Société Nationale des Chemins de fer Français), particularly in short span bridges, that led to deterioration of track conditions and loss of ballast bed stability due to high vibrations. SNCF's measurements indicated that acceleration levels ranging from *0.7g* to *0.8g* (ERRI D 214/RP 9 (1999)) resulted in track-related issues, such as the formation of voids under the sleepers, loss of ballast compaction and particles, track alignment issues and excessive concrete cracking.

Following this, experiments were carried out at the German Federal Institute for Materials Research and Testing (BAM), conducted by the ERRI Committee D214 (ERRI D 214/RP 8, 1999) to further explore the impact of high accelerations on the behaviour of ballast on bridges (Rücker and Rohrmann (1998)). The experiment involved simulating a ballasted track by utilizing a 3m long steel box embedded with four rail-connected sleepers. This setup was subjected to various vertical acceleration amounts, reaching up to *1g*, whose frequencies ranged from *2 Hz* to *20 Hz*, this setup confirmed previous SNFC studies, affirming that accelerations exceeding *0.7g* lead to the loss of interlock of the ballast layer (Baeßler and Rücker, 2007). After conducting these

experiments, the ERRI committee suggested the limits to maximum vertical deck accelerations for ballasted and ballast-less tracks, the former in order to preserve the ballast stability, while the other to prevent the loss of wheel-rail contact. The limit values are, respectively, 3.5 m/s^2 and $5m/s^2$.These limits were derived from a safety factor of 2 and are currently incorporated in EN 1990 Annex (2001).

In order to replicate these experiments, a smaller test rig held at BAM was built as described by Zacher and Baeßler, (2008). This rig involves a 1.05x1.05 steel box filled with ballast, containing an embedded sleeper, with both subjected to vertical vibrations through a servo-hydraulic shaker, as illustrated in Figure 2.15.

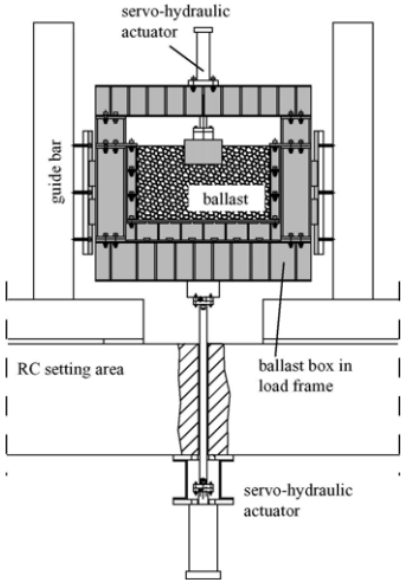

Figure 2.15: Test set-up for the shake table with combined loading (Zacher and Baeßler, 2008)

The box is subjected to vertical vibrations up to $2g$ and frequencies up to 60 Hz, while the sleeper, after compaction, experiences loads up to 20 KN at a frequency of 1 Hz, with acceleration measurements taken in the box ab and in the sleeper as.

Figure 2.16 illustrates both transfer functions, showcasing the dependence on both amplitude and frequency of the box acceleration. The left diagram represents the transfer function from the larger box (test rig used by the D214 committee of experts from ERRI) , considering amplitudes of $1g$ and frequencies up to 20 Hz, while the right diagram shows the transfer function from the smaller box. Comparing both figures, it can be concluded that the interested frequency range was achieved, meaning that the small test rig results are comparable and can be utilized for further analysis.

Subsequently, the settlement of the sleeper was measured, as illustrated in Figure 2.17.

Figure 2.17 shows the settlements of the sleeper in a test with a vibration frequency of 12 Hz. After preloading, sequences were run with shaking of the box (grey areas). For each acceleration level, the system underwent 50 cycles of base acceleration, followed by 20 cycles of sleeper

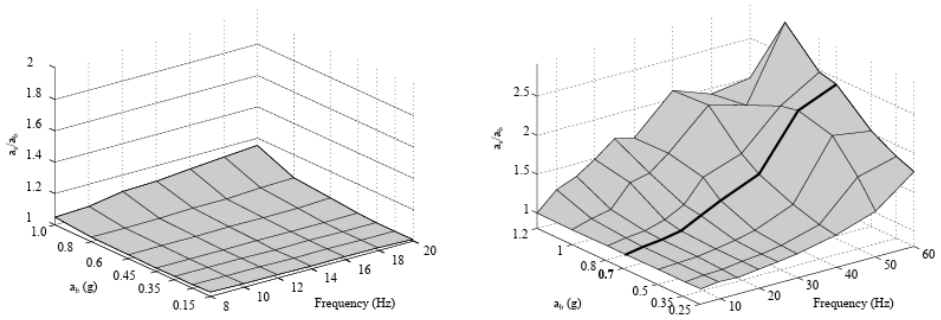

(a) Box A (b) Box B

Figure 2.16: Transfer function sleeper/box (adapted from Zacher and Baeßler, 2008)

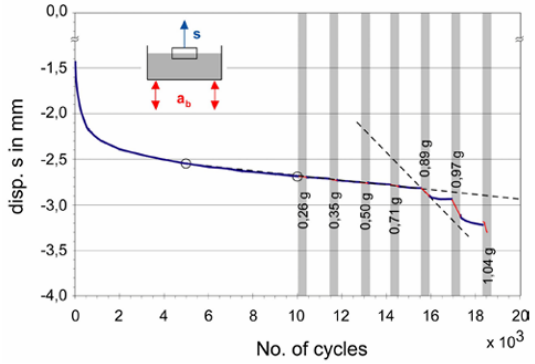

Figure 2.17: Vertical displacements for a test with vibrations at f = 12 Hz (Matthias and Rücker, 2007)

loading for each acceleration level, with this sequence being repeated 20 times consecutively to ensure measurable effects. Following that, the ballast was preloaded again, and the process was repeated for the next shake table acceleration level. Analysing the figure, it becomes evident that settlements are barely affected by vibrations up to an amplitude level of *0.71 g*. It is observed once again that acceleration amplitudes exceeding *0.7 g* lead to track-related issues.

2.5 Lateral Displacement of Sleepers on Vibrating Bridge Decks

2.5.1 Introduction

In the previous section, the discussion was focused on the impact of vertical accelerations on ballasted tracks, leading in ballast fabric loosening and permanent sleeper deformations. As mentioned earlier, the crucial safety concern is defined by the lateral behaviour of the track, where lateral resistance is compromised due to vibrations in the bridge deck. This adds complexity to the classic track stability problem (imperfect track loaded by longitudinal forces due to high temperatures), introducing the potential reduction of lateral resistance caused by bridge deck vibrations. In

this chapter, the track stability problem will be addressed not only by considering vertical bridge deck accelerations but also by examining the lateral forces acting on embedded sleepers. This comprehensive approach will provide a more detailed understanding of how both vertical and lateral forces influence track stability.

2.5.2 Track stability

Due to variations in temperature and the passage of railway traffic, considerable longitudinal compression forces can be induced in the continuous welded rail (CWR) track. The track is prone to lateral shift and buckling due to these forces. Therefore, the track's lateral resistance is essential to prevent this lateral displacement from occurring. Another, relevant scenario where the track tends to shift laterally is in curved track sections, where centrifugal forces act during the passage of railway traffic.

When the rail temperature increases above the rail's neutral temperature, normal forces N_T are induced in the rails. Figure 2.18 illustrates the relationship between the increase of the rail temperature and the lateral displacements. If there are no additional disturbances, the lateral displacement increases as the temperature rises from 0 to A. Once T_{max} is reached at the snap-through point A, the track buckles and changes its position to the next equilibrium at A". Point B, between T_{max} and T_{min}, represents the path in the diagram with additional disturbances, such as the rolling of a vehicle. Starting from position B, this displacement is reversible as long as point B' is not reached. If the disturbance is too great, the lateral displacements may also lead to sudden snap-through to point B". When T_{min} is reached, under appropriate external loads, the track might buckle to a different equilibrium point. Theoretically, T_{min} represents the critical temperature limit (Esveld, 1998). However, the observed T_{min} temperatures do not correspond to common railway practices, so engineers typically adopt a more conservative or higher T_{min} threshold in their designs. For a track of poorer quality, point C' can also be reached directly on the path from 0 to C'.

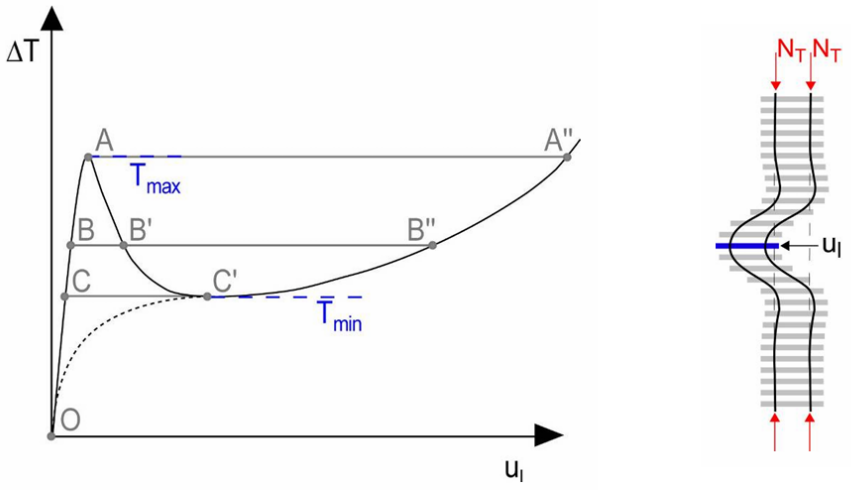

Figure 2.18: Lateral shift u_1 of the track following an increase of the rail temperature ΔT relative to the neutral temperature (Baeßler et al. (2012))

Additionally, Kish et al. (2013) summarized all the parameters that affect the formation and growth of misalignment's leading to track buckling, as depicted in Table 2.8.

	Event	Major Casual Factors
1	Formation of initial track misalignments	(1) High L/V's and logitudinal forces (2) Reduced local track resistance (3) Initial imperfections (welds) and defects
2	Growth of misalignments	(1) L/V increase due to imperfections (2) Increase in longitudinal forces (3) Track "dynamic uplift" due to vertical loads (4) Many cycles of L/V's
3	Buckling	(1) High longitudinal force (2) Reduced Tn (Stress-free temperature) (3) Misalignments generated by track shift (4) Dynamic uplift wave (5) Weakend lateral resistance

Table 2.8: Track lateral stability mechanism as summarized by Kish et al. L and V are the lateral and vertical forces acting on the track (adapted from adapted from Baeßler (2008))

2.5.3 Vibration-induced creep phenomenon

The lateral resistance of the track is defined by the ballast's behaviour, when subjected to lateral movements. This behaviour, influenced by the ballast's physical properties and the manner in which it is installed, has been studied through lateral displacement resistance tests both in-situ and on test stands. Consequently, these tests help determine a force-displacement curve, where two scenarios, in response to lateral displacements, can be seen: the behavior of the track with well-consolidated ballast (Figure 2.19 a)) and the behavior of the track with the freashly tamped ballast (Figure 2.19 b)) (Kish and Samavedam, 2013).

- Peak Lateral Resistance, F_P, and corresponding displacement, w_P
- Limiting Lateral Resistance, F_L, and corresponding displacement, w_L

For weak or recently maintained tracks, tests have shown that $F_P = F_L$ and $w_P = w_L$

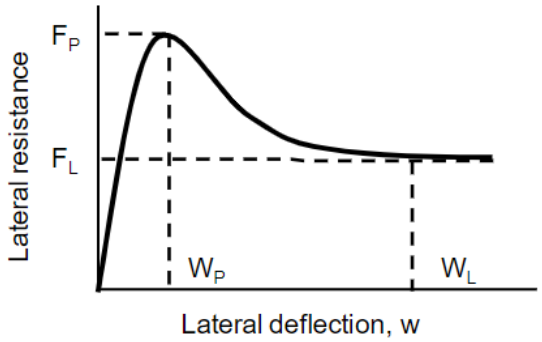

a) Consolidation track

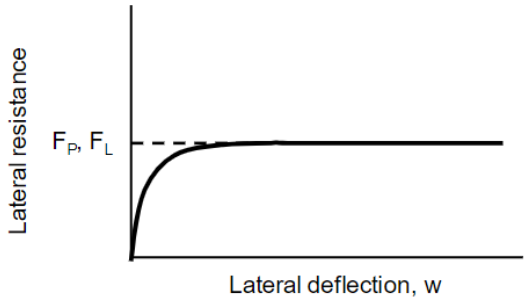

b) Freshly Tamped

Figure 2.19: Typical Lateral Resistance Characteristics (Kish and Samavedam, 2013)

The sleeper bottom surface roughness is an important parameter as it determines the component of the base resistance. The lateral resistance is primarily ensured by the ballast surrounding the sleeper and the friction forces generated between the surfaces of the sleepers and the ballast. Therefore the lateral resistance can be expressed as the sum of the base (F_b), side (F_s), and end (F_e) shoulder resistance components of the sleeper, as depicted in Figure 2.20:

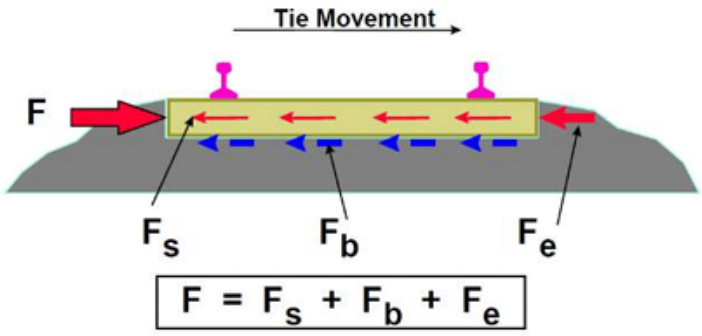

Figure 2.20: Components of the lateral resistance at the sleeper-ballast interface (Fra, 2003)

The resistance force, F_s, mainly derives form the spacing between sleepers, the interlocking ability form the ballast and the friction developed between the lateral surface of the sleeper and the ballast. Force, F_e, primarily depends on the geometry and the amount and quality of the ballast in

the "shoulder" area. In case of force, F_b, laboratory test show that the characteristics of the sleeper (type, weight, and dimensions), the vertical load and the height of the "shoulder ballast" are the parameters that most influence the final value of this resistance.

In (Van, 1997) it is stated that the contribution of the three components to the total lateral resistance is distributed equally, with each representing 1/3 of the total. However, with sufficiently large vibration excitation amplitudes, the material behavior of the ballast bed changes. When the dynamic wheel loads act through the track structure onto the ballast bed, and the bridge deck is excited to vibrations, it results in the ballast bedding being subjected to base excitation. This causes the ballast to loose it´s strength propertied, which may potentially lead to a sudden lateral displacement of the track structure. This phenomenon could be called "vibration-induced creep" as suggested by Baeßler (2008). However, to capture the influence of dynamic loading and the development of permanent deformations is challenging. Lateral displacement resistance tests are generally conducted under slow force application, but when dynamic loading occurs simultaneously over the sleeper and the subgrade, the rate at which the sleeper shifts becomes a significant factor. In tests on individual sleepers, where vibrations are additionally introduced over the sleeper in addition to increasing the force acting on the sleeper head, permanent displacements increase significantly (see Figure 2.21)

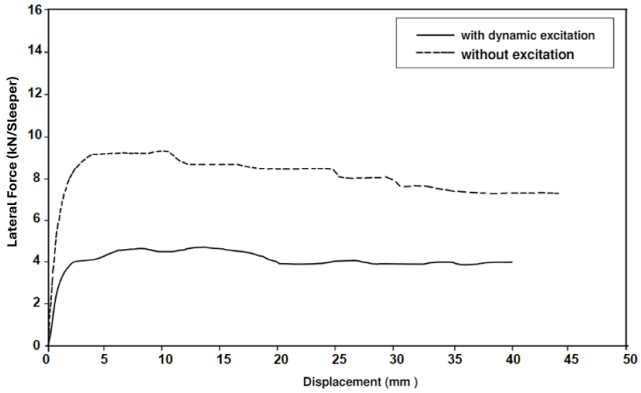

Figure 2.21: Comparison of a test with dynamic excitation on the sleeper to tests without dynamic excitation (ERRI D202 - RP7)

Figure 2.21 shows how the "vibration-induced creep" phenomenon impacts the lateral displacement of the sleeper. However, the application of the test results cannot be further assessed because the test parameters for describing the dynamic loading and the advancement rate of the sleeper are not specified in the publication. Given the lack of experimental test data to assess the "vibration-induced creep" phenomenon, Baeßler (2008) investigated this issue for the special case of a ballast superstructure with dynamic base excitation. The tests were conducted in shaker boxes with the aim of:

- Understanding the behavior of the sleeper-ballast system under combined dynamic loading
- Determining whether the lateral resistance is reduced by the dynamic excitation

- Describing the displacement development of the sleeper, especially in the area of a few oscillation cycles
- Investigating whether displacements significantly increase only after reaching a threshold amplitude under constant preload
- Providing a mathematical relationship for the displacement accumulation of the sleeper

2.5.4 Past test models

In order to better investigate the "vibration-induced creep" phenomenon, Baeßler and Rücker (2008), conducted the testing of a laterally loaded sleeper on a shake table (see Figure 2.22). In the test set-up the box is excited vertically from the top with a load actuator via a steel girder that distributes the loading to the sides of the box. Additionally, the sleeper, which is surrounded by ballast, is loaded laterally with a constant compressive load on one end of the sleeper using a second actuator.

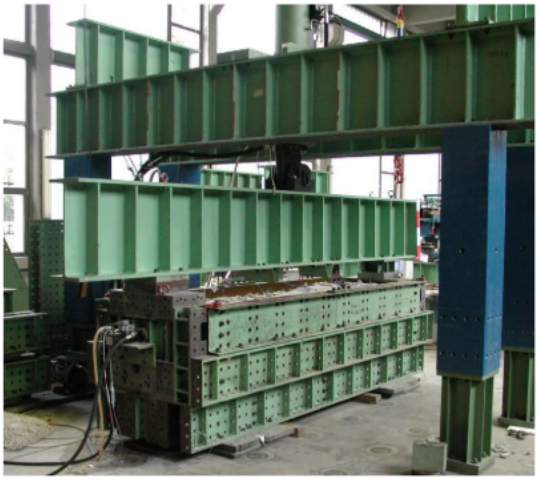

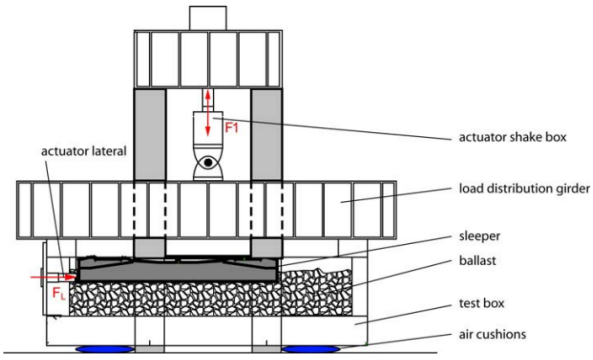

Fig. 10. Test rig for lateral resistance on vibrating shake table

Figure 2.22: Test rig for lateral resistance on vibrating shake table (Baeßler, 2008)

The placement of the sleeper-ballast system was done in two stages. Firstly, the ballast was placed and vibrated until the sleeper settlement stabilised. Secondly, vertical preload of 1000 load cycles was applied directly on the sleeper to stabilize the contact between the sleeper and the ballast bed.

The test consist in combining shake table vibrations along with a lateral load of the sleeper. The tests were performed with constant lateral load, F_L, and a specified acceleration amplitude a_{Box} for 500 consecutive cycles. All the tests, were performed as multi-stage tests, with the vibration amplitude incrementally increased every 500 cycles, while all other parameters remained fixed. For each test sequence, the horizontal preload, ranging from 0.5 to 2.0 kN was kept constant.

Figure 2.23 shows the lateral displacement of the sleeper as a function of the lateral load and acceleration magnitude. It displays the results of completed tests for different lateral preloads, where a clear relationship between the sleeper displacement, the preload, and the vibration amplitude can be noted. The test results depicted in Figure 2.24 demonstrate great repeatability. The graphical representation provides the displacement of the sleeper, where a clear correlation between the sleeper displacement and both the preload and vibration amplitude is again noted. Within the range of 500 cycles, the lateral movement of the sleeper can be approximated by a linear relationship between displacement and the number of load cycles (see Figure 2.24).

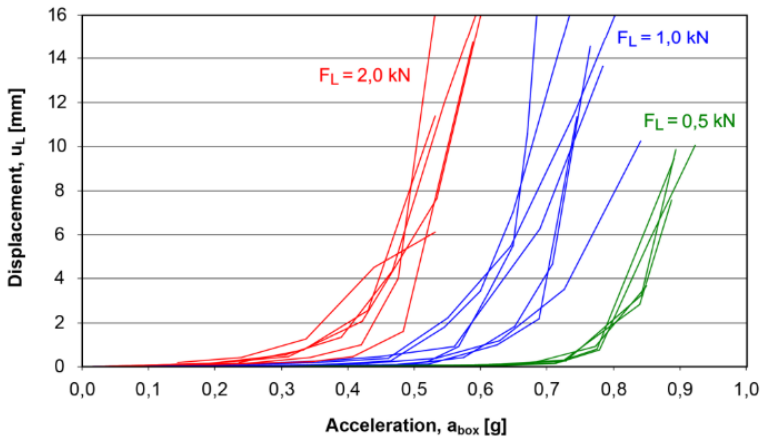

Figure 2.23: Accumulated sleeper displacements after 500 cycles of box vibration in dependence of the magnitudes of lateral load F_L and box acceleration a_{box} (Baeßler, 2008)

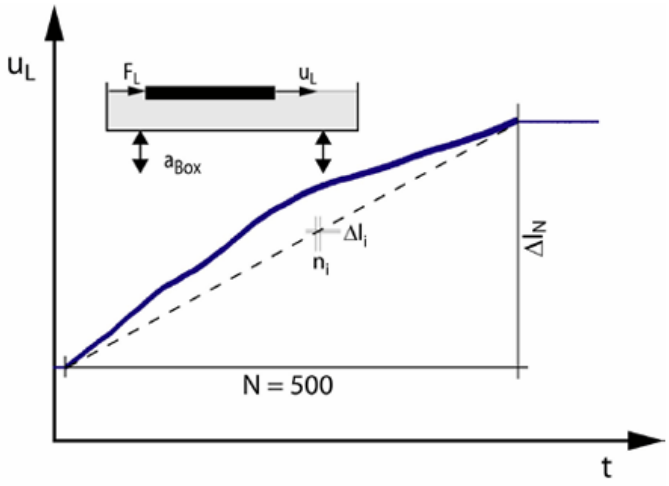

Figure 2.24: Linearized increments in test sequences of 500 consecutive cycles a_{Box} (Baeßler, 2008)

Based on an idealised rheological model (Figure 2.25) and on the test results shown above, a mathematical form can be given for a vibration induced creep behaviour dependent on the number of load cycles instead of time. This combined element including a spring and a dashpot connected in series was then used for the numerical model of the lateral sleeper support. The numerical model will be explained in detail in section 3.3.1.

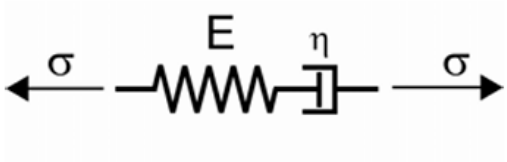

Figure 2.25: Maxwell-element as a rheological model relating the axial solicitation σ and deformation through the spring stiffness E and dashpot viscosity η (Baeßler, 2008)

The empirical creep formula to approximate the vibration-induced creep is given by:

$$\Delta l_n = \text{sign}\left(\frac{F_L}{F_{L0}}\right) \cdot C_1 \cdot \left|\frac{F_L}{F_{L0}}\right|^{C2} \cdot e^{C3 \cdot \frac{a}{a_0}} \cdot n \tag{2.15}$$

where Ci are constants, F_L is the lateral sleeper force, a is the acceleration amplitude, and n is the number of load cycles (Baeßler, 2008). F_{L0} is a reference force used to normalize applied forces, while a_{L0} is a reference acceleration used to scale acceleration terms, ensuring the equations remain general and dimensionally consistent across various loading and dynamic conditions. It is important to highlight that the formula is restricted to the conditions and parameters of this particular system.

Additionally, Zacher and Baeßler (2008) conducted an additional analysis, regarding the influence of higher frequencies on the lateral displacement. Using a smaller test rig (see Figure 2.26).

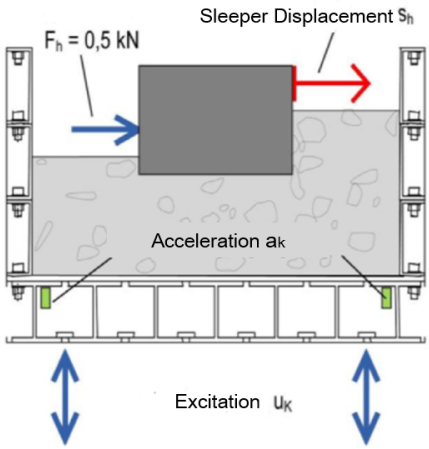

Figure 2.26: Test setup for dynamic loading with lateral load (adapted from (Baeßler, 2008)

The lateral displacements of the sleeper after 500 acceleration cycles were plotted against the acceleration amplitudes at different frequencies, as shown in Figure 2.27.

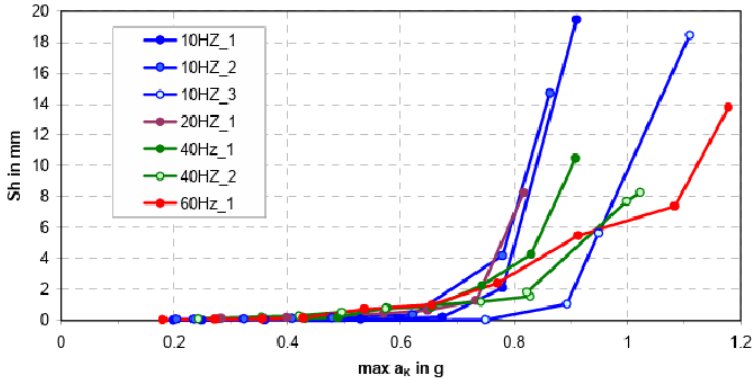

Figure 2.27: Lateral displacements of the sleeper after 500 acceleration cycles at different amplitudes and frequencies (Zacher and Baeßler, 2008)

With the representation of tests encompassing frequencies ranging from 10Hz to 60Hz, the authors effectively demonstrated, in accordance with the conclusions from the previously mentioned laboratory experiments, that for amplitudes below 0.7g the impact is relatively small. However, under high accelerations, after 500 cycles, the displacement reaches approximately 20 mm (0.4mm per cylce), so Zacher and Baeßler (2008) recommend that, exceptionally, accelerations values above the current limits could be permitted, for 10 vibration cycles. Specifically, the researchers suggest reducing the safety factor from 2 to 1.3 (in alignment with the German soil loading capacity), allowing maximum accelerations of 0.55g for ballasted tracks and 0.75g for ballastless tracks. On top of that, the experiments indicate that lateral displacements are independent of the frequency, as no distinct pattern is noticed across the different frequency levels.

2.6 Methods for analyzing the dynamic behaviour of the structure and vehicle

In this section an overview of different existing methods for analyzing the dynamic response of the structure and railway vehicles is presented. The addressed methods are: i) the method of moving loads, in which the vehicle is modeled as a set of moving loads, of fixed magnitude, representing the static load of each axle; ii) the vehicle-structure interaction methods, iterative and direct, in which the bridge and the train interact with each other as a coupled dynamic system.

2.6.1 Moving loads model

This method is based on a simplified representation, where the vehicles actions over the structure are defined as a set of moving loads representing the static load of each wheelset (Goicolea and Gabaldón, 2012). Consequently the train is represented as set of constant moving loads, Fi, spaced according to the train's geometry, as depicted in Figure 2.28. This method neglects the interaction between the vehicle and the structure, therefore it is only focused for the study of the dynamic response of the structure.

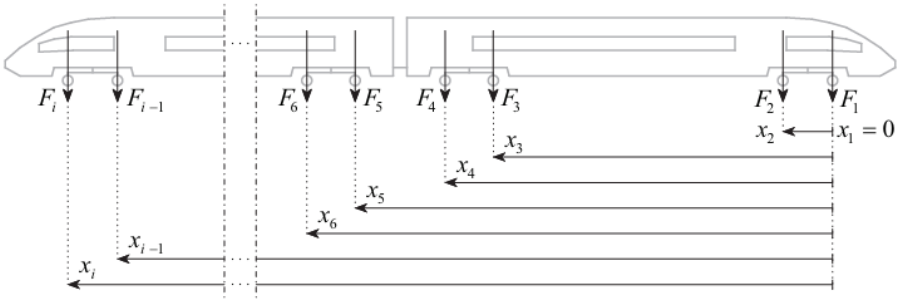

Figure 2.28: Moving loads model (Montenegro, 2015)

The dynamic response of the structure can be determined by solving the following dynamic equation of motion:

$$\mathbf{Ma} + \mathbf{Ca} + \mathbf{Ka} = \mathbf{F}_{ext} + \mathbf{F}_i \tag{2.16}$$

where **M**, **C** and **K** are the mass, damping and stiffness matrices of the structure, respectively, F_{ext} are the externally applied nodal loads and F_i are the time-dependant moving loads associated with the static weight of the vehicle that act on the structure, as illustrated in Figure 2.28.

Equation (2.16) can be solved utilizing direct integration methods like the Newmark method (Nikitas et. al, 2012), or using the modal superposition method (Chopra, 1995). Direct integration methods provide solutions for both linear and nonlinear models, whereas the modal superposition method is usually restricted to linear systems.´Modal analysis possesses a distinct advantage in its flexibility to select the number of modes to consider, thereby excluding high-frequency components associated with higher modes that may not significantly impact the bridge's response.

Consequently, this approach leads to a significant reduction in computational costs. However, the direct time integration of the complete system provides a more general approach, which can be essential in certain scenarios, such as when considering nonlinear effects or contacts (Goicolea and Gabaldón, 2012).

2.6.2 Vehicle-structure interaction methods

2.6.2.1 Iterative method

In order to analyse the dynamic response of the vehicle-structure interaction, an iterative solution method is applied (Yang and Fonder, 1996). This method consists in dividing the vehicle and track coupling system into two separate substructures, vehicle and structure (Lei and Noda, 2002). This methodology is based on establishing the equilibrium of forces at the contact interface between the train and the bridge and, additionally, using an iterative procedure to apply the constraint equations, which relate the displacements of the contact nodes of the vehicle to the corresponding displacements of the structure (Delgado and Santos, 1997). By modeling the two subsystems as separate structures, the following system of equations may be expressed as:

$$\begin{bmatrix} \mathbf{M}_S & \mathbf{0} \\ \mathbf{0} & \mathbf{M}_V \end{bmatrix} \begin{bmatrix} \ddot{\mathbf{a}}_S \\ \ddot{\mathbf{a}}_V \end{bmatrix} + \begin{bmatrix} \mathbf{C}_S & \mathbf{0} \\ \mathbf{0} & \mathbf{C}_V \end{bmatrix} \begin{bmatrix} \dot{\mathbf{a}}_S \\ \dot{\mathbf{a}}_V \end{bmatrix} + \begin{bmatrix} \mathbf{K}_S & \mathbf{0} \\ \mathbf{0} & \mathbf{K}_V \end{bmatrix} \begin{bmatrix} \mathbf{a}_S \\ \mathbf{a}_V \end{bmatrix} = \begin{bmatrix} \mathbf{F}_S \\ \mathbf{F}_V \end{bmatrix} \tag{2.17}$$

where M, C and K are the mass, damping and stiffness matrices, respectively, a are the nodal displacements, F is the load vector and the letters s and v represent structure and vehicle, respectively.

The iterative method developed by Delgado and Santos (1997), assumes that the vehicle-structure interaction occurs exclusively at a single point, between the rail and the vehicle wheel, with interaction forces acting only in the vertical direction, and that the train wheels are always in contact with the rail. Therefore, the method contains the following assumptions: i) The moving loads applied to the structure at iteration i+1, corresponding to each axis (see Figure 2.29), are decomposed into two components, the static load of the wheelset F_{sta} and the dynamic component of the interaction force F^i_{dyn}, as illustrated in equation 2.18. With the previously calculated dynamic component (F^i_{dyn}), it is possible to solve the system of equations corresponding to the structure (see equation (2.17)) to obtain the displacements of the structure under the contact nodes $\mathbf{a}^{i+1}_Y$.

$$F^{i+1}_s = F_{sta} + F^i_{dyn} \tag{2.18}$$

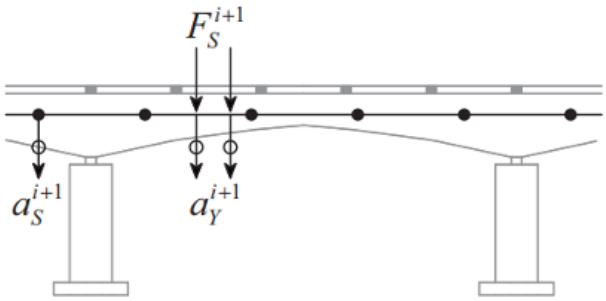

Figure 2.29: Scheme of the the vehicle-structure interaction problem (Montenegro, 2015)

ii) With the displacements of the vehicle $\mathbf{a}_V^{i+1}$ (see Figure 2.30), which correspond to the displacements of the structure under the contact nodes $\mathbf{a}_Y^{i+1}$ and taking into account the irregularities (r) that may exist between the wheel and the rail, the following equation can be verified:

$$a_v^{i+1}(t) = a_s^{i+1}(t) + r \tag{2.19}$$

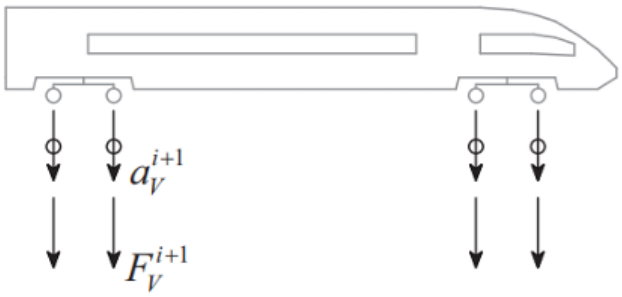

Figure 2.30: Scheme of the the vehicle-structure interaction problem (Montenegro, 2015)

iii) Therefore, by solving the system of equations corresponding to the structure (see equation (2.17)) it is possible to determine the dynamic component of the interaction force F_{dyn}^{i+1} to be applied to the structure in the next iteration, once:

$$F_{dyn}^{i+1}(t) = F_v^{i+1}(t) \tag{2.20}$$

Finally, it is necessary to verify, at the end of each interaction, the following convergence criterion:

$$\frac{\left\| F_{dyn}^{i+1} - F_{dyn}^{i} \right\|}{\left\| F_{dyn}^{i} \right\|} \leq \varepsilon \tag{2.21}$$

where where ε is a specified tolerance. If the desired level of convergence is reached, the procedure can proceed to the next time step, otherwise, the iterative process continues.

2.6.2.2 Direct method

The direct method, developed by Neves et al. (2012) involves coupling the dynamic equilibrium equations of the vehicle and the structure with additional constraint equations that establish a direct correlation between the displacements of the contact nodes on the vehicle with the corresponding nodal displacements of the structure, not allowing separation between them. This method considers the irregularities at the contact interface in the constraint equations and both the vehicle and structure subsystems may be modelled with various types of finite elements, regardless of their complexity. Consequently, the equations of motion and the constraint equations from a single system can be solved avoiding the previously mentioned interactions (Section 2.6.2.1) and can be expressed by the following expression:

$$\begin{bmatrix} \overline{\mathbf{K}}_{FF} & \overline{\mathbf{D}}_{FX} \\ \overline{\mathbf{H}}_{XF} & \mathbf{0} \end{bmatrix} \begin{bmatrix} \mathbf{a}_F^{t+\Delta t} \\ \mathbf{X}^{t+\Delta t} \end{bmatrix} = \begin{bmatrix} \overline{\mathbf{F}}_F \\ \bar{\mathbf{r}} \end{bmatrix} \tag{2.22}$$

where $\bar{\mathbf{K}}_{FF}$ is the effective stiffness matrix of the vehicle-structure system, $\overline{\mathbf{D}}_{FX}$ is the transformation matrix that associates the contact forces in the local coordinate system with the nodal forces in the global coordinate system. $\overline{\mathbf{H}}_{XF}$ is the transformation matrix that relates the nodal displacements of the structure in the global coordinate system with the displacements of the auxiliary points defined in the local coordinate system. The nodal displacements and the contact force are defined as $\mathbf{a}_F^{t+\Delta t}$ and $\mathbf{x}^{t+\Delta t}$, respectively, $\bar{\mathbf{F}}_F$ is the load vector and $\bar{\mathbf{r}}$ are the irregularities at the contact interface.

Later Neves et al. (2014) extended the formulation to allow the separation between wheel and rail by incorporating a nonlinear problem-solving algorithm.

2.6.2.3 Lateral interaction method

The methods mentioned in the previous sections don't take into account the lateral interactions between the wheel flange and rail, which can significantly affect the dynamic behavior of the system. In order to address this limitation, it is necessary to consider the geometries of the wheel and rail profiles and employ a fully nonlinear formulation. According to Shabana et. al (2007), the wheel-rail contact problem can be divided into two separate approaches: i) The *constraint contact formulation* approach, uses kinematic constraints equations, that do not allow the separation or penetration between the wheel and the rail (Shabana et. al (2007); ii) The second approach named *elastic contact formulation* defines the normal contact force as a function of the penetration between the wheel and the rail (Shabana et al. (2004) and Pombo et al. (2007)).

There are other methods that deal with the formulation of the wheel-rail contact problem, namely the On-line and off-line wheel/rail contact algorithm (Sugiyama et al. (2009)). In the offline approach, contact points are determined beforehand through geometric analysis and stored

in a lookup table for later use in dynamic analysis. On the other hand, the online method calculates contact points using iterative procedures at every time step during dynamic analysis.

It is also worth noting that the contact problem can be categorized into normal and tangential contact. The normal contact problem, in which the normal contact forces are computed, is based on the Hertz theory (Hertz, 1882). According to this theory, the elastic deformation of the steel of the wheel and the rail creates an elliptic contact area. The tangential contact problem was originally formulated by Kalker (Kalker, 1967), with the development of the linear theory of rolling contact.

Chapter 3

Applied methods

3.1 Initial considerations

High-speed railway bridges have particular dynamic characteristics and the trains themselves are structures with their own dynamic properties, running over and interacting with the bridge. The interaction between moving trains and the bridge can lead to resonance effects, amplifying the bridge´s dynamic response. Such amplified responses are particularly concerning due to their potential impact on the stability of the ballast and therefore the support of the track.

In this chapter the methods used to analyze the resonance effects caused by dynamic loads on high-speed railway bridges and their consequences on the ballast stability are discussed. Specifically, how the vertical deck accelerations, induced by single train passages, from various HSLM-A trains, affect the lateral stability of the ballast. Additionally, the chapter will address ballast behavior by constructing curves that relate different vertical acceleration amplitudes to the resulting ballast instability, providing a more detailed understanding of the impact on the lateral track stability.

3.2 Moving Loads Method

The study of the dynamic response of the bridge under the action of railway traffic was carried out considering the train as a set of moving loads as depicted in Figure 3.1. and implemented in MATLAB (2024). Since this method focuses on the behaviour of the bridge, it provides more efficient results and demands less computational effort compared to interaction methods (Ribeiro, 2004).

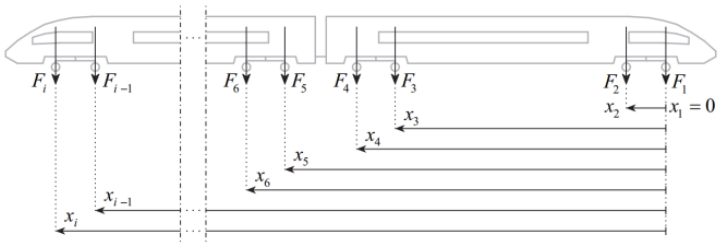

Figure 3.1: Representation of the loads in the moving load model (Montenegro, 2015).

3.2.1 Formulating the dynamic problem

Considering the train loads as a set of moving loads **F**(t) applied externally to the bridge, where each degree of freedom of the structure must be in equilibrium in any given moment of time *t*, the dynamic problem can be defined by the following equation:

$$\mathbf{F}_i(t) + \mathbf{F}_d(t) + \mathbf{F}_e(t) = \mathbf{F}(t) \tag{3.1}$$

where $\mathbf{F}_i$ are the inertial forces, $\mathbf{F}_d$ are the damping forces and $\mathbf{F}_t$ are the elastic forces. This forces can be defined by the following expressions:

$$\mathbf{F}_i(t) = \mathbf{M}\ddot{\mathbf{u}}(t) \tag{3.2}$$

$$\mathbf{F}_a(t) = \mathbf{C}\dot{\mathbf{u}}(t) \tag{3.3}$$

$$\mathbf{F}_e(t) = \mathbf{K}\mathbf{u}(t) \tag{3.4}$$

where **M**,**C**,**K** are the mass, damping and stiffness matrices, respectively and $\ddot{u}$,$\dot{u}$ and u are acceleration, velocity and displacement vectors.

Given this, equation 3.1 can be rewritten as:

$$\mathbf{M}\ddot{u}(t) + \mathbf{C}\dot{u}(t) + \mathbf{K}u(t) = \mathbf{F}(t) \tag{3.5}$$

Clough and Penzien (1975) define a Rayleigh damping matrix as a linear combination of the mass and stiffness matrices:

$$\mathbf{C} = c_1\mathbf{M} + c_2\mathbf{K} \tag{3.6}$$

with the constants *c1* and *c2* being determined from the following system of equations:

$$\begin{Bmatrix} c_1 \\ c_2 \end{Bmatrix} = 2\frac{\omega_m \times \omega_n}{{\omega_n}^2 - {\omega_m}^2} \times \begin{bmatrix} \omega_n & -\omega_m \\ -\frac{1}{\omega_n} & -\frac{1}{\omega_m} \end{bmatrix} \times \begin{Bmatrix} \xi_m \\ \xi_n \end{Bmatrix} \tag{3.7}$$

where ω_n and ω_m are the angular frequencies and ξ_n and ξ_m are the damping coefficients corresponding to the n-th and m-th vibration modes of the structure, respectively.

3.2.2 Definition of Moving Loads

In a finite element model, more than knowing the position of each point load at any given moment of time, it is necessary to obtain the equivalent nodal loads on a path intended for a load to travel in. By defining the temporal load functions at the nodes along the path of the moving loads, the resulting equivalent nodal forces can be obtained. These nodal forces represent the effect of the moving loads as they move across the bridge, as illustrated in Figure 3.2. To determine these temporal load functions $x_k(t)$, the nodes along the path of the moving loads are initially identified, and the position of each load P_k in relation to the starting node of the path $x_k(t_0)$ is determined. Following this, the position of each load for every time instant t is determined by adding an incremental distance equal to $v \times t$ to the initial position, with v being the velocity of the train. This process is expressed by the following equation:

$$x_k(t) = x_k(t_0) + v \times t \tag{3.8}$$

To conclude the process, the load P_k and and it´s corresponding position x_k for each time instant t are converted into a equivalent nodal force, as follows:

$$P_i = P_k \times N_i(x_k) \tag{3.9}$$

with $N_i(x_k)$ is a shape function associated with node i of the structure, defined as:

$$N_i(x) = \begin{cases} \frac{x_k - x_{i-1}}{L_{i-1,i}}, x_{i-1} \leq x_k \leq x_i \\ 1 - \frac{x_k - x_i}{L_{i,i+1}}, x_i \leq x_k \leq x_{i+1} \end{cases} \tag{3.10}$$

where $L_{i-1,i}$ and $L_{i,i+1}$ are the distances between node i and node $i+1$, respectively.

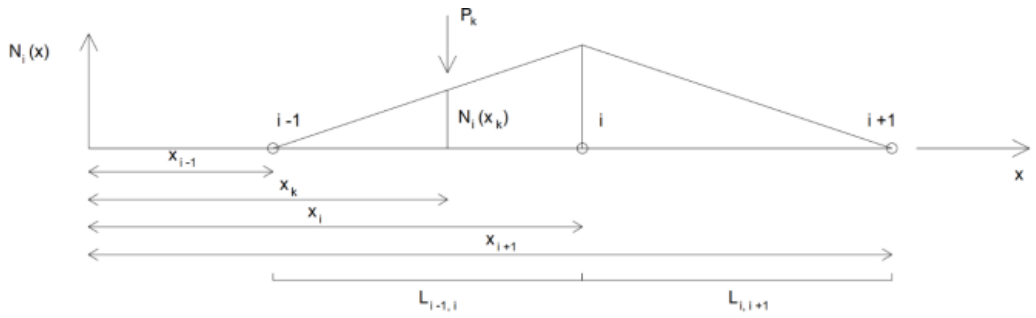

Figure 3.2: Variation of the nodal force at node i due to the load P_k, (Montenegro, 2008)

3.2.3 Modal Superposition Method

In the present work, the dynamic equilibrium equations are solved using the modal superposition method. Solving the system of Eq.3.5 using a direct time-integration algorithm, each time step $t+1$ is dependent on the structural response at the previous time step t, which means that

the analysis has to be performed with a single computation process. In complex structures with a large number of DOF, such as bridges, this process can escalate the computational cost and be very time consuming. As an alternative the modal superposition method translates the dynamic problem into a representation of itself using modal coordinates, which stand for the contribution of each vibration mode to the total response (Chopra, 1995; Clough and Penzien, 2003). This approach functions by using a set of independent equations, each with a single unknown variable, which is the modal coordinate y. Considering the N mode shapes φ, a structure's free vibration can be described as:

$$u(t) = \sum_{i=1}^{N} \varphi_n \cdot y_i \tag{3.11}$$

Given that a mode's vibration, whose natural frequency is ω can be described by:

$$y_n(t) = A_n \cos \omega_n + B_n \sin \omega_n \tag{3.12}$$

the time variation of the structure's displacement can be written as:

$$\mathbf{u}(t) = \varphi_n(y_n(t) = A_n \cos \omega_n + B_n \sin \omega_n) \tag{3.13}$$

which gives

$$\left[\mathbf{K} - \omega_n^2 \mathbf{M}\right] \varphi_n = 0 \tag{3.14}$$

Taking into account the orthogonality properties of the modes, it can be observed that when any matrix is multiplied on the left by a transposed modal vector and on the right by a different modal vector, the resulting values is a scalar of 0. For instance, considering the mass matrix M as an example, and the distinct modes n and m:

$$\varphi_n^T \mathbf{M} \varphi_m = 0 \tag{3.15}$$

Consequently, the scalars M_n, C_n and K_n, known as the generalized mass, damping and stiffness for mode n, respectively, can be obtained by using:

$$M_n = \varphi_n^T \mathbf{M} \varphi_n \tag{3.16}$$

As such, the uncoupled equation takes the form of:

$$M_n \cdot \ddot{y}_n + C_n \cdot \dot{y}_n + K_n \cdot y_n = F_n(t) \tag{3.17}$$

which produces N equations with the single unknown y_n:

$$\ddot{y}_n + 2 \cdot \xi_i \cdot \omega_n \cdot \dot{y} + \omega_n^2 \cdot y_n = \frac{F_n(t)}{M_n} \tag{3.18}$$

This method offers a computational advantage by allowing s structure´s dynamic response to be characterized with a finite number of modes, which can be selected through an initial analysis.

Moreover, the efficiency of the modal superposition method is further increased because the required number of modes to accurately represent the dynamic response of the structure is generally lower than the N number of DOF.

3.3 Methodology for Evaluating Ballast Stability

3.3.1 Past Studies Background

As mentioned, this study was based on past experimental test performed by BAM. In order to gain a better understanding of the growth of rail misalignment's, Baeßler (2008) modelled a continuous welded track rail track as a beam structure, supported by lateral springs (Figure 3.3). The calculations were done for a maximum of 500 consecutive vibration cycles with constant amplitude and a lateral shift of 1 mm was defined as the reference value. All calculations were conducted in an ANSYS-Environment. The relevant parameters, adapted from Van (1997), are presented in Table 3.1. It is important to note, that this case study is solely based on the calculations of these exact parameters. This is especially important for variables such as the normal forces N_T, which are induced by this specific temperature difference ΔT.

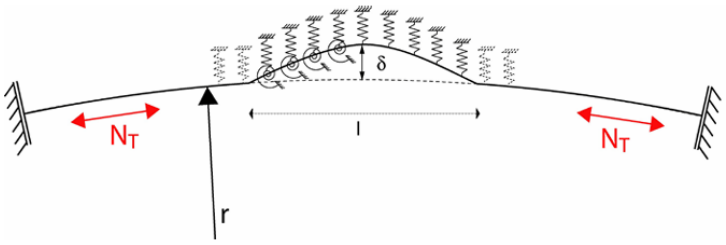

Figure 3.3: Mechanical model for lateral stability of track section (adapted from Baeßler, 2008)

Parameter	Value	Dimension
Radius r	5 000	m
Track length l_g	48	m
Sleeper Distance	0.6	m
Torsional Stiffness	170 000	Nm/rad per m
Amplitude of Misalignment δ	0.005	m
Length of Misalignment l_δ	10.0	m
Temperature ΔT	40	K
Lateral Peak Resistance at Sleeper	8	kN

Table 3.1: Parameters of the mechanical model (adapted from Baeßler, 2008)

In the presented model, UIC 60 rails are assumed, and the vertical loads from the vehicle as well as the longitudinal stiffness are neglected. The lateral support of the track is modelled as the Maxwell combination of a spring and a damper (as mentioned in section 2.5.4), representing the sleepers under lateral forces.

The springs placed at the rail support points have a non-linear elastic behaviour and each sleeper is supported by a combination of a spring and a creep element (damper) (see Figure 2.25), with both elements being described as non-linear elastic. To address the vibration induced-creep phenomenon each damper incorporates the creep equation, Eq. 2.15.

Furthermore, an additional assumption in the calculations is the alignment between the peak misalignment amplitude and the peak of the vibration mode, as shown in Figure 3.4. Additionally, the vibration modes are assumed to demonstrate sinusoidal behavior.

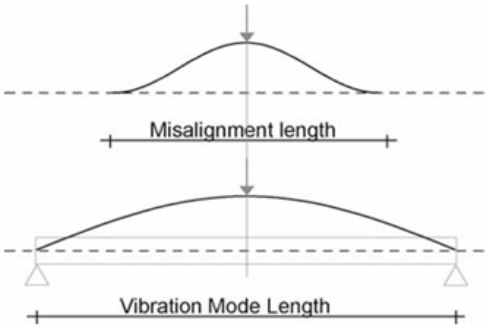

Figure 3.4: Assumption for configuration of misalignment peak and vibration mode peak (Baeßler and Rücker, 2007)

Baeßler (2008) used the described mechanical model to determine the increase in track alignment error under various influencing factors (such as high temperatures, a larger track alignment error and high bridge deck accelerations). In this thesis, the primary influencing factor under analysis are the vertical bridge deck accelerations. The calculations were done for a maximum of 500 consecutive cycles with a constant amplitude of 0.8g and 0.4g.

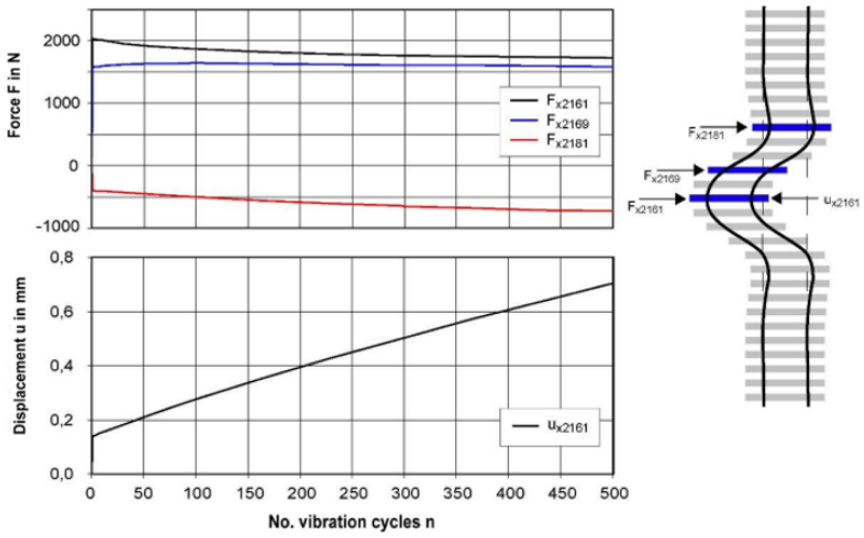

Figure 3.5: Lateral Forces and displacements of the track for vibrations of a bridge deck with amplitudes of a = 0.4 g (Baeßler, 2008)

In Figure 3.5 , forces and displacements due to bridge deck vibrations with an amplitude of 0.4g are represented. As the accelerations amplitudes initiate, which act as the vibration-induced creep within the model, the misalignment gradually rises. As a result of the creep phenomenon, the force at the middle node (node 2161) slightly decreases, which makes the ballast redistribute the load, reducing the force it bears at this point, and transferring the loads to the adjacent sleeper (node 2169). Across the 500 cycles of vibration, a constant increase of 0.55 mm is noted, as the forces on the ballast show little variation over time.

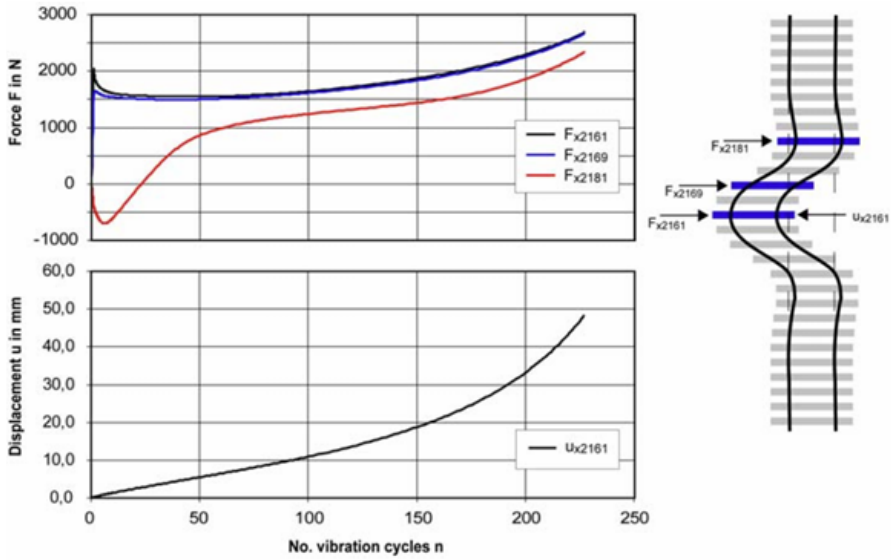

Figure 3.6: Lateral Forces and displacements of the track for vibrations of a bridge deck with amplitudes of a = 0.8 g

Figure 3.6 shows the results for an amplitude of 0.8 g, where a completely different scenario emerges. The forces at the middle node (node 2161) decreases rapidly and the load is absorbed by the sleeper at a further outward node (node 2181). It is noted that after 50 cycles the forces experience another significant increase, which lead to a subsequent rise in displacements. This continuous increase of deflections, coupled with the rise of lateral forces, leads to a loss of lateral stability in the track.

3.3.2 Adjusting Traditional Methods Based on Past Experiments

The two described graphs from the past experiments, presented in the previous subsection, verify the dependency that lateral displacements have on the vibration amplitude. In this study both graphs were recreated in MATLAB, as illustrated in Figures 3.7 and 3.8. The purpose of recreating these graphs was to calculate the number of cycles required to achieve a 1 *mm* lateral shift of the ballast bedding.

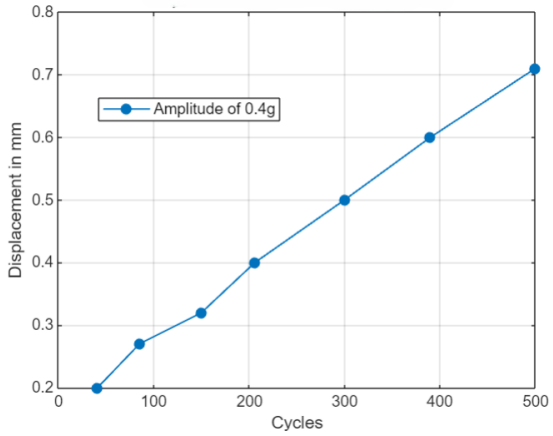

Figure 3.7: Displacements for amplitudes of 0.4g

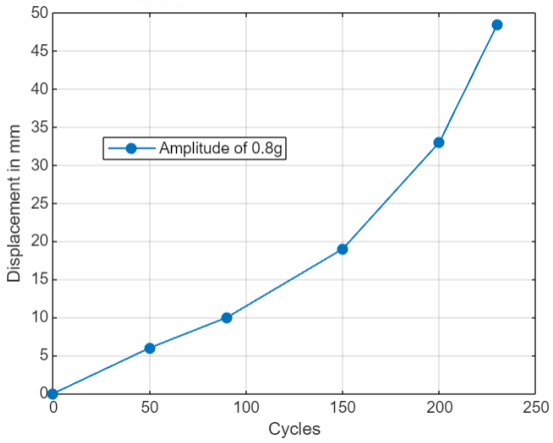

Figure 3.8: Displacements for amplitudes of 0.8g

In the subsequent phase of the research, an "Accumulated Track Displacement Curve" will be developed, based on the existing fatigue strength curves ("S-N" curves). Traditionally, Fatigue Strength curves plot the stress against the number of cycles to failure, however, in this study, instead of stress, acceleration will be plotted against the number of cycles. This analysis employs concepts similar to fatigue analysis to evaluate the accumulation of damage in ballast. Unlike traditional S-N curves that deal with fatigue over multiple cycles, this analysis is similar to fatigue but specifically addresses the accumulation of damage from a single dynamic analysis. Here, the focus is on a single train passage, rather than multiple passages as in conventional fatigue analysis. In order to build this "Accumulated Track Displacement Curve", a displacement of 1 *mm* was defined as the failure criteria, which indicated that the *0.4g* amplitude graph reached failure at 764.55 cycles, while for the *0.8g* graph, failure occurred at 10.62 cycles. Using these two data points, (10.62 cycles, 0.8 g) and (764 cycles, 0.4 g), the modified S-N curve was constructed and implemented in MATLAB, as depicted in Figure 3.9.

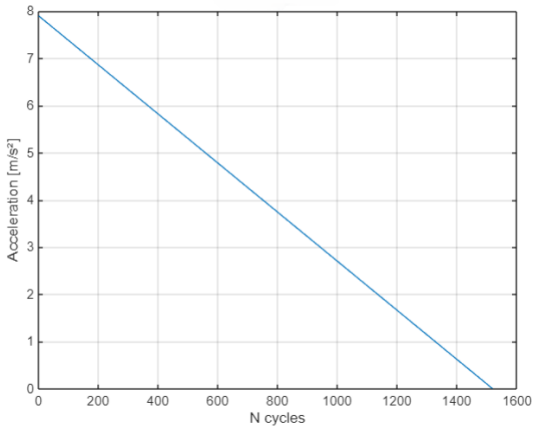

Figure 3.9: Accumulated Track Displacement Curve

The equation of the curve is the following:

$$y = -0.0052x + 7.9 \tag{3.19}$$

With the Accumulated Track Displacement Curve it becomes possible to evaluate the number of cycles required to reach failure for any given acceleration amplitude. The traditional method of S-N curves will be discussed in detail in the next section. Traditional fatigue analysis considers the cumulative damage over many load cycles, often spanning the entire service life of a structure. In contrast, this study focuses on the immediate accumulation of damage from a single train passage, which can be sufficient to induce instability in the ballast.

3.3.3 Practical Implementation

Given the fact that there are no established methods for assessing the vibration induced-creep under fatigue conditions, additional representation of the data was developed in order to identify the most reliable method for predicting the ballast lateral stability. For this purpose, two additional graphs were constructed and implemented in MATLAB: one using a logarithmic-logarithmic (log-log) scale and the other using a linear-logarithmic (lin-log) scale.

Figure 3.10 presents the logarithmic-logarithmic graph, which plots the number of cycles on logarithmic scale against a logarithmic scale for acceleration amplitudes. Typically, S-N curves are modelled by fitting the experimental results of merged datasets using a linear regression method known as the least-square fit, which minimizes the differences between observed and predicted values (International Journal of Fatigue, 2021). The linear regression method, implies taking the stress range ($\Delta\sigma$) as a dependent variable, $y = \log_{\Delta\sigma}$, and the number of cycles as the independent variable, $x = logN$, the mean fatigue S-N curve is obtained by estimating both the slope m and the intercept log *Const* (Baptista C. 2016):

$$Const = \Delta\sigma^m N \Rightarrow \log \mathbf{N} + \mathbf{m} \log \Delta\sigma = \log \mathbf{Const} \Rightarrow y = b - a \cdot x \tag{3.20}$$

Solving this equation for $y = \log \Delta\sigma$, we get:

$$\log \Delta\sigma = -\frac{1}{m} \cdot \log N + \frac{1}{m} \cdot \log Const \tag{3.21}$$

In this case instead of stress, acceleration amplitude is the dependant variable, so the equation is expressed as:

$$\log \Delta Acc = -\frac{1}{m} \cdot \log N + \frac{1}{m} \cdot \log Const \tag{3.22}$$

Since we have the initial "Accumulated Track Displacement Curve" (lin-lin S-N curve) in the format $y = b - a \cdot x$ (Eq. 3.19), the following correspondences can be made:

- *log N* serves as the *x*-variable
- The term $\frac{1}{m}$ is equivalent to the slope m of the Accumulated Track Displacement Curve
- The term $\frac{1}{m} \cdot \log Const$ represents the *y*-intercept b of the Accumulated Track Displacement Curve.

Given these relationships, the slope m and constant *Const* are determined, and have the following values:

Parameter	**Value**
m	6.165
Const	3 482 760.026

Table 3.2: Determined values of the slope m and constant Const.

By inserting these values to the original equation, Eq. 3.20, the Accumulated Track Displacement Curve with a logarithmic-logarithmic scale is obtained:

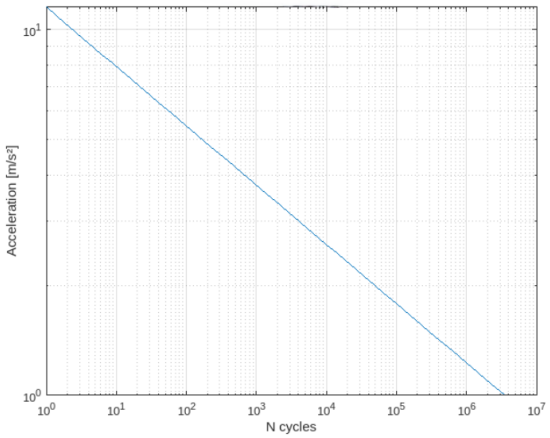

Figure 3.10: Accumulated Track Displacement Curve Log-Log Scale

While this method aligns with the conventional fatigue analysis methods, it does not necessarily guarantee accurate results for this case study. Traditional Fatigue Strength curves are also

typically plotted in a logarithmic-logarithmic scale. However, constructing these S-N curves involves conducting numerous tests to realistically estimate the material's lifespan over millions of cycles. In this study, only data from two tests (Figure 3.7 and Figure 3.8) are available. Consequently, transitioning from a linear scale to a logarithmic scale extends the x axis from values initially observed at 1500 cycles over to values relevant for millions of cycles. As a result, one graph compared to the other may be conservative due to the limited experimental data, making it challenging to achieve highly accurate results.

The linear-logarithmic graph (Figure 3.11) offers another insight by plotting the number of cycles on a logarithmic scale against a linear scale for acceleration amplitude. This approach is seen as the most effective, as it ensures consistency and comparability with past BAM tests, where a lin-log scale was also utilized.

The equation of the logarithmic-logarithmic curve (Eq. 3.20) was constructed in a format, where both the x-axis and y-axis are scaled logarithmically. However, to develop a curve in a linear-logarithmic format, only the x-scale (which represents the number of cycle N) is modified, while the y-axis (representing acceleration amplitude, ΔAcc) remains linear.

In this lin-log transformation, the equation is adjusted as follows:

$$\log N = \text{Const} - m \cdot \Delta Acc \tag{3.23}$$

By repeating the process used in the log-log curve, the equation is solved for x = log N and the slope m and constant $Const$ were again calculated using the initial Accumulated Track Displacement Cruve (lin-lin), resulting in the following equation:

$$\Delta Acc = \frac{1}{m} \cdot \log N + \frac{Const}{N} \tag{3.24}$$

The values, m and $Const$, were again inserted to the original equation, Eq. 3.23, and the Accumulated Track Displacement Curve with a linear-logarithmic scale was obtained:

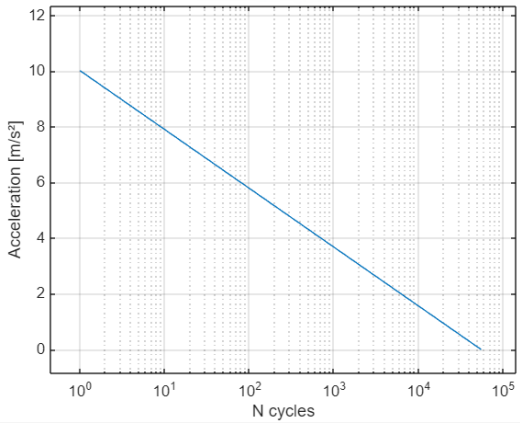

Figure 3.11: Accumulated Track Displacement Curve Lin-Log Scale

Displaying all three graphs together allows for a more insightful comparison of how different

scaling methods affect the representation and interpretation of the data. Figure 3.12 illustrates the three Accumulated Track Displacement Curves together, allowing a better understanding of the variations between the curves and how their values differ distinctly.

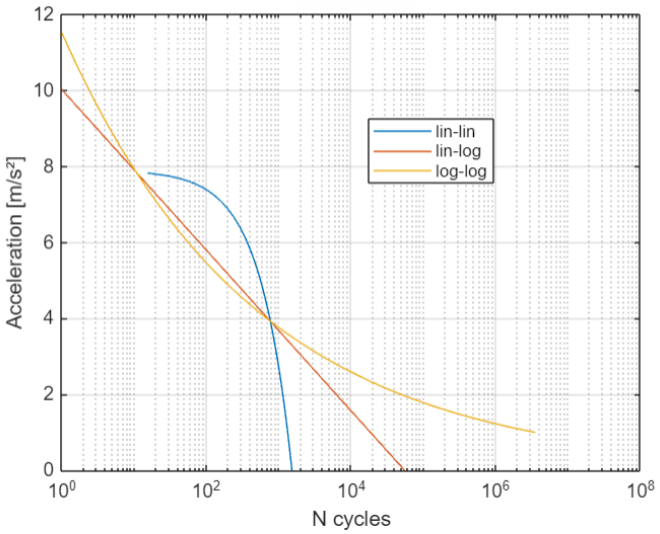

Figure 3.12: All Accumulated Track Displacement Curves side by side

In order to relate the impact of a single train passage to the results from past experiments and simulations, fatigue analysis methods, such as Rainflow-Counting and the Palmgren-Miner damage accumulation rule were used through MATLAB.

The Rainflow Counting was conducted on the Acceleration-Time history of single train passages, in order to evaluate the cyclic loading experienced by the ballast. Subsequently, with the Accumulated Track Displacement Curves and the Rainflow-Counting method it was possible to apply the Palmgren-Miner rule, to assess the cumulative damage sustained by the ballast. Both of these methods will undergo a more comprehensive analysis in the next section. It is important to note again that these methods are traditionally applied to Stress-Time ($\sigma - t$) diagrams. However,in this study, Acceleration-Time ($a - t$) diagrams were analyzed, meaning acceleration amplitudes were used in place of stress amplitudes.

3.4 Damage accumulation method

3.4.1 Initial Considerations

Although this analysis draws an analogy to fatigue, it is fundamentally different in its approach. Traditional fatigue analysis considers the cumulative damage over many load cycles, often spanning the entire service life of a certain material. In contrast, this study focuses on the immediate accumulation of damage from a single train passage, where a acceleration spectrum form a single dynamic analysis is employed.

3.4.2 Rainflow-Counting

In this study, the rain-flow counting method was employed for the fatigue analysis of one single train passage. Traditionally, this method consists in the relation between the stress σ and the strain ε, because the fatigue damage is particularly affected by the alternate plastic deformations (Fatigue of Metallic Materials, 1992). This approach involves, converting stress-time history diagrams (see Figure 3.13 a)) in stress-strain diagrams (see Figure 3.13 b))., which shows the hysteresis cycles to which the element is subjected.

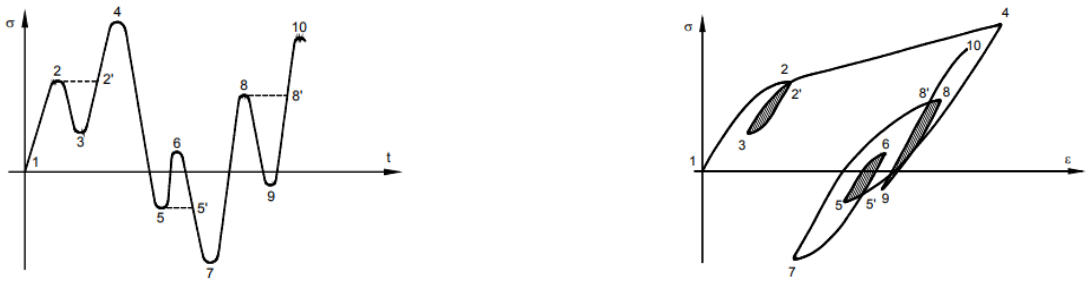

a) b)

Figure 3.13: Representative loading diagrams: a) $\sigma - t$; b) $\sigma - \varepsilon$ (adapted from Frýba (1996))

The method obtained its name from an idea that water is flowing along a pagoda-shaped roof. To better visualize this method, the $\varepsilon(t)$ diagram must be rotated by 90° (time-axis downwards, as illustrated in Figure 3.14. In this representation, only the local extremes are represented, with the valleys designated by odd numbers and the peaks by even numbers.

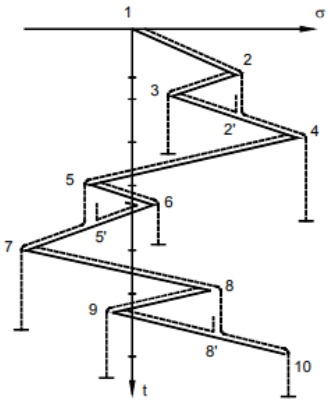

Figure 3.14: Rainflow Method (adapted from Frýba (1996))

Based on the diagram shown in Figure 3.14, the water movement can proceed either from the left to right or in the reverse direction, always starting from each peak or valley. The drop begins its movement at point 1, travelling along the first roof until it reaches a peak or valley. At that moment, the drop falls vertically until it reaches another roof, with its trajectory being interrupted when:

a) if it intersects a drop that is falling from an upper roof, as seen in the path 3-2´, which intersects the path of the drop that is falling vertically from point 2.

b) passes through a point where the stress is greater than or equal (in absolute values and of the same type, peal or valley) to the stress at the point where it began its route, as we can see in peak 6 and valley 3. The path 5-6 ends after 6 because valley 7 is greater (in absolute value) than 5. Similarly, the route ends at 3 because peak 4 is higher than peak 2.

A new path is not started until the previous one has been completed. Therefore, each completed path (1-2-2'-4; 4-5-7; 7-8-8'-10) is counted as half cycle, and two half-cycles with the same stress amplitude form a full cycle. The interruptions in the path, such as 2-3-2', 5-6-5', and 8-9-8' count as complete cycles.

This method allows to convert the Stress-time history of Figure 3.13, in a $\sigma - t$ diagram, with the stress ranges being paired into complete stress cycles, as depicted in Figure 3.15.

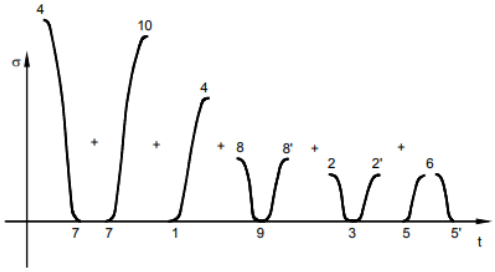

Figure 3.15: $\sigma - t$ diagram equivalent with stress-time history in Fig.3.3 (adapted from Frýba (1996)

3.4.3 Fatigue Strength curves

The fatigue resistance of a material is generally defined using the traditional Fatigue Strength Curves (S-N curves). The S-N curves, also known as Wöhler Lines, typically represent the relationship between the stress amplitude (S) applied to a material and the number of cycles (N) that the material can endure before reaching failure.

These curves were obtained from experimental tests results on materials subjected to cyclic loading with constant stress amplitude, and are usually expressed by the following relationship:

$$N = C\Delta\sigma^{-m} \tag{3.25}$$

where, $\Delta\sigma$ is the stress amplitude ranges, N is the number of stress cycles and C and m are the constants of the curve determined experimentally.

Typically, S-N curves are represented by a series of $log(\Delta\sigma)$-$log(N)$ curves, obtaining:

$$logN = logC - mlog\Delta\sigma \tag{3.26}$$

Whose representation in double logarithmic scale corresponds to a straight line.

The Fatigue Strength Curves are traditionally defined by a fatigue strength reference value at 2 million cycles, $\Delta\sigma_C$, a constant amplitude fatigue limit, $\Delta\sigma_D$, and a cut off limit $\Delta\sigma_L$. In Figure 3.16 a typical fatigue Strength Curve is illustrated:

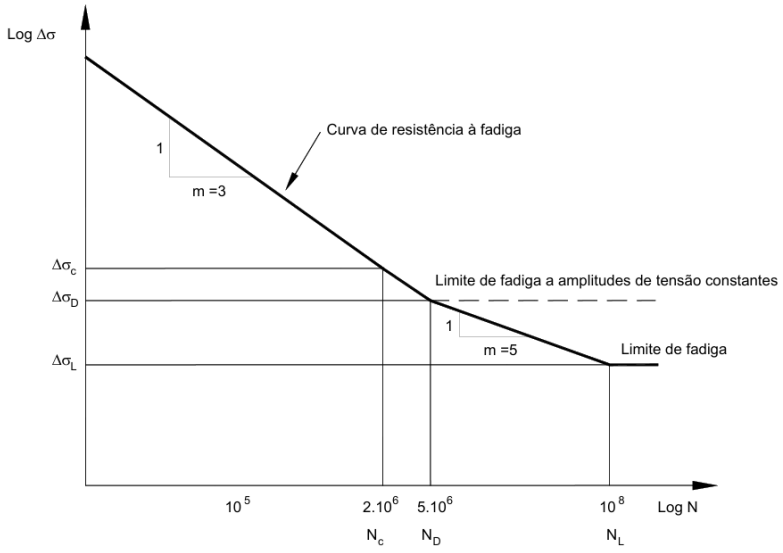

Figure 3.16: Typical Fatigue Strength Curve (adapted from Tembe (2001)

The Figure shows that when a material is subjected to cyclic loading with a constant amplitude lower than $\Delta\sigma_D$, it can endure an infinite number of cycles without developing fatigue failure. In case of loadings with stress amplitudes below and above $\Delta\sigma_D$, the higher stresses with lead to the development of the initial crack, which results in a reduction of $\Delta\sigma_D$ over time. Consequently, more cycles with an amplitude below $\Delta\sigma_D$ will contribute to the propagation of the crack. However, the contribution of cycles with these lower amplitudes is not infinite, as there exists a limit value, $\Delta\sigma_L$, below which fatigue failure will never occur, regardless of the number of cycles it is subjected to, known as the cut-off limit.

3.4.4 Stress Spectrum

The passage of trains over a bridge induce various stress variations in all structural elements. These variations are traditionally represented using stress-time diagrams ($\sigma - t$). By applying specific counting methods to the stress history, it is possible to assess the number of stress cycles a specific element undergoes, with each cycle being associated with different stress amplitude classes. Through this counting process, a histogram with the frequency of each amplitude can be obtained. This stress spectrum (see Figure 3.17), provides a good understanding of how often each stress amplitude occurs, which is crucial for evaluating the fatigue behavior of the structural elements.

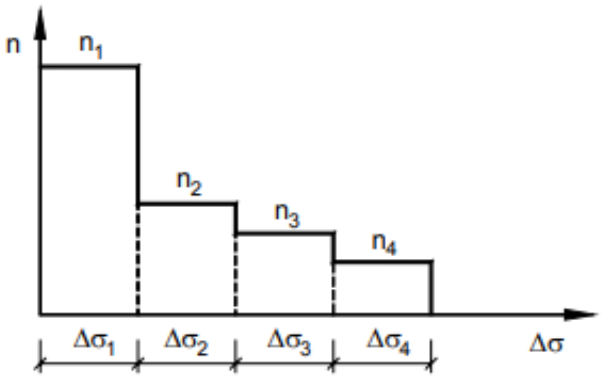

Figure 3.17: Stress Spectrum (EN 1993-1-9, 2005)

The stress amplitudes, $\Delta\sigma$, represent the difference between the highest stress value (σ_{max}) and the minimum stress value (σ_{min}), within a specific time period,

$$\Delta\sigma = \sigma_{max} - \sigma_{min} \tag{3.27}$$

For the stress counting process, the previously stated, Rain-flow counting method was used in this study.

3.4.5 Palmgren-Miner accumulative criterion

In fatigue analysis, the accumulated damage (D) in a material due to a certain load is measured. For a load with a constant amplitude, damage is defined as the ratio between the number of applied cycles (n) and the total number of cycles that would lead to fatigue failure (N):

$$D = \frac{n}{N} \tag{3.28}$$

If the material or structure is subjected to a stress spectrum with different levels of amplitudes ($\Delta\sigma_i$, n_i), the partial damages corresponding to each amplitude can be calculated as:

$$D_i = \frac{n_i}{N_i} \tag{3.29}$$

where N_i is obtained from the S-N curve (see Figure 3.18)

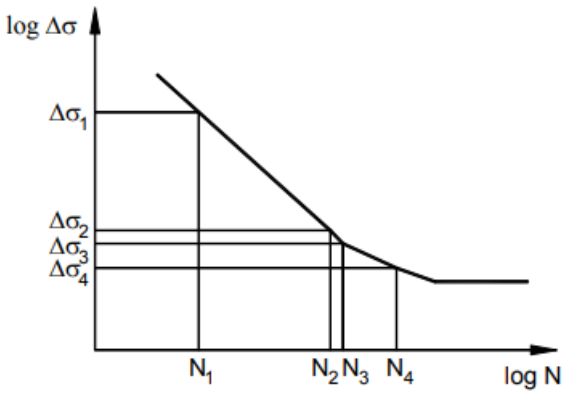

Figure 3.18: S-N curve (adapted from EN1993-1-9 (2005)

According to Palmgren and Miner the damage induced to each loading cycle can be linearly accumulated. This means that if a material is subjected to various stress levels during its operational lifespan, the total damage can be calculated by summing the damage fractions attributed to each stress level, as expressed by the following equation:

$$D = \sum_{\mathrm{i}} \frac{n_i}{N_i} \tag{3.30}$$

According to this method failure is predicted to occur when $D = 1$, therefore when the sum of the damage fractions equals to one, the material has reached it´s fatigue life.

The entire process can be visualized step-by-step by the flowchart, presented in Figure 3.19. It illustrates all the methodologies used in this case study, from collecting acceleration-time histories to calculating cumulative damage using the Palmgren-Miner Rule.

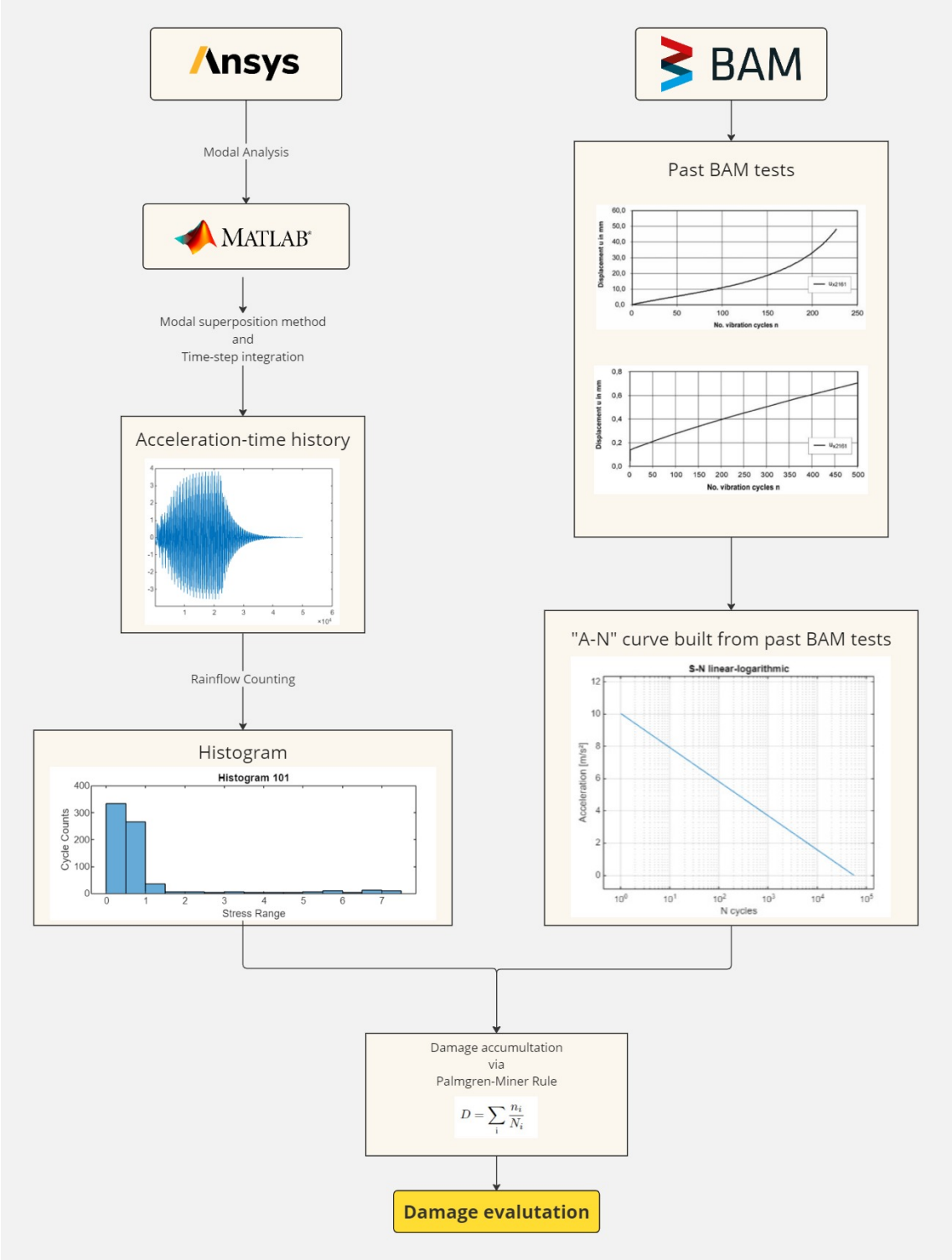

Figure 3.19: Flowchart of the study's methodology

Chapter 4

Case Study

4.1 Introduction

In the present chapter, the bridge model and its parameters, developed using ANSYS, are presented in Section 4.2. This section provides a detailed description of the bridge and includes the vibration modes derived from the modal analysis. Section 4.3 shifts focus to the train models used in the study. It offers a characterization of each train model and outlines the resonant speeds selected for the dynamic analysis conducted in MATLAB.

Subsequently, Section 4.4 presents the results from the dynamic simulations, with a particular emphasis on the maximum accelerations at the mid-span of the deck resulting from single passages of the HSLM-A load models. The chapter concludes with an examination of the methods employed to evaluate damage accumulation from these single passages. This is followed by the presentation of various graphs with cut-off values in Section 4.5, aimed at assessing which acceleration amplitudes contribute most significantly to damage.

4.2 Bridge Finite Element

4.2.1 Modelling assumptions and Parameters

A 10-meter simply supported bridge was modeled in ANSYS using the BEAM3 finite element. The BEAM3 element is suitable for 2D elastic beam and truss modeling, making it ideal for this type of structural analysis. The bridge was modeled as a simply supported slab, as illustrated in Figure 4.1.

Figure 4.1: Bridge Model Developed in ANSYS

The bridge was modeled with the specified dimensions and material properties to accurately represent the structural behavior under load. The parameters used for modeling the bridge were sourced from Arvidsson et al. (2019). Table 4.1 presents all the parameters used in the finite element model.

Slab bridges (original cross-sections)		
L (m)	m (tonne)	EI (GNm^2)
10	15.4	12.5

Table 4.1: Mass and stiffness for simply supported bridges (adapted from Arvidsson et al. (2019))

where, L is the span length, m is the mass and EI is the Young's modulus, E (GPa), multiplied by the moment of inertia, I (m^4).

4.2.2 Natural Frequencies and Mode Shapes

To obtain the natural vibration modes of the studied bridge, a modal analysis was performed on the bridge model. This analysis identifies the significant vibration modes that are crucial for assessing vertical accelerations. The first three vertical modes are shown in Figure 4.2. The corresponding frequencies for these modes are listed in Table 4.2.

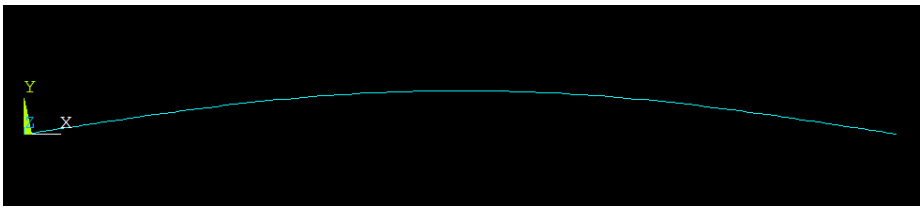

a) 1st vertical vibration mode

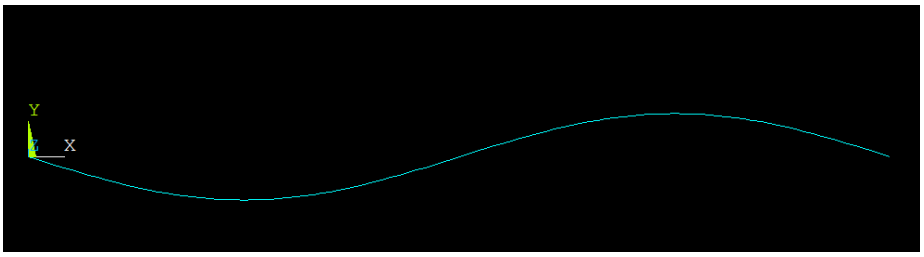

b) 2nd vertical vibration mode

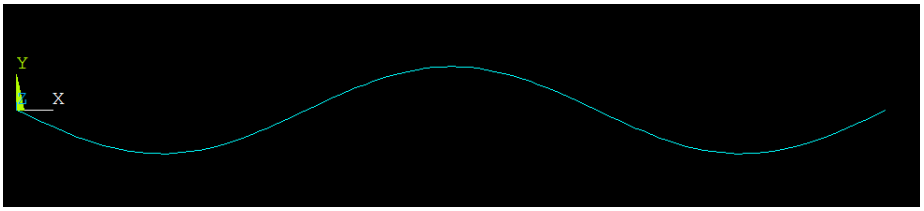

c) 3rd vertical vibration mode

Figure 4.2: Vertical vibration modes of the bridge

Frequencies (Hz)	
First vibration mode	14.1
Second vibration mode	56.7
Third vibration mode	127.4

Table 4.2: Natural vibration frequencies of the first vertical vibration modes of the studied bridge

4.3 Dynamic analysis of High-Speed Trains

This section presents the dynamic analysis performed on all the HSLM-A trains (HSLM-A1 until HSLM-A10), applying the modal superposition method, which was implemented using MATLAB. The bridge was subjected to train speeds ranging from 140 km/h to 420 km/h. Although, a design speed of 350 km/h was assumed, by applying a uncertainty factor of 1.2, it increases the maximum speed to 420 km/h. Conducting the analysis at speeds up to 420 km/h was deliberate choice to evaluate the bridge´s behaviour under more extreme conditions, where resonance effects are more likely to occur.

4.3.1 Specifications and characteristics of the Trains

In this subsection, the configuration of all HSLM-A load models (mentioned in section 2.2.2) is illustrated in Figure 4.3, and the properties are shown in Table 4.3.

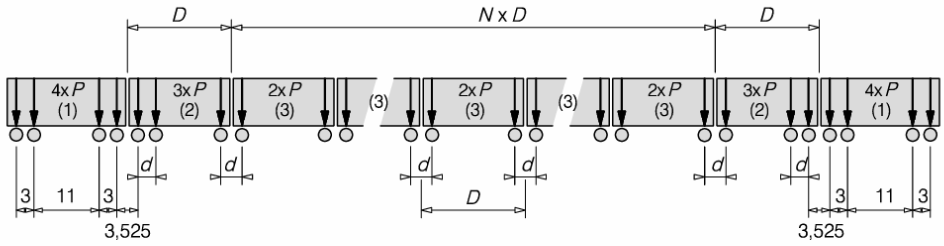

Key
(1) Power car (leading and trailing power cars identical)
(2) End coach (leading and trailing end coaches identical)
(3) Intermediate coach

Figure 4.3: HSLM-A configuration (EN1991-2, 2017)

Universal Train	Number of intermediate coaches N	Coach length D [m]	Boogie axle spacing d [m]	Point force P [kN]
A1	18	18	2,0	170
A2	17	19	3,5	200
A3	16	20	2,0	180
A4	15	21	3,0	190
A5	14	22	2,0	170
A6	13	23	2,0	180
A7	13	24	2,0	190
A8	12	25	2,5	190
A9	11	26	2,0	210
A10	11	27	2,0	210

Table 4.3: HSLM-A' properties (adapted form EN1991-2, 2017)

4.3.2 Resonance effect

Resonance is the phenomenon that involves the transfer of energy from one vibrating system to another when the frequency of the first matches the natural frequency of the second. In railway traffic, this phenomenon occurs at speeds above 200 km/h and can have severe consequences for the structure, as it amplifies the dynamic response and, consequently, the potential damage to the structure.

In this case, as the structure is represented as a simply supported beam, the resonant speeds (v_{res}) of the trains can be estimated using the following sentence:

$$v_{res} = n_j \frac{D}{i} \tag{4.1}$$

where n_j is the natural frequency of the bridge, D is the coach length and i is an integer. The ratio of the last two indicates the length over which the excitation occurs.

Therefore, by using equation 4.1 the following resonant speeds were obtained and organized on table 4.4:

	Speeds (km/h)				
Trains	i=1	i=2	i=3	i=4	i=5
HSLM-A1 (D=18 m)	913,68	456,84	304,56	228,42	182,74
HSLM-A2 (D=19 m)	964,44	482,22	321,48	241,11	192,89
HSLM-A3 (D=20 m)	1015,20	507,60	338,40	253,80	203,04
HSLM-A4 (D=21 m)	1065,96	532,98	355,32	266,49	213,19
HSLM-A5 (D=22 m)	1116,72	558,36	372,24	279,18	223,34
HSLM-A6 (D=23 m)	1167,48	583,74	389,16	291,87	233,50
HSLM-A7 (D= 24 m)	1218,24	609,12	406,08	304,56	243,65
HSLM-A8 (D= 25 m)	1269,00	634,50	423,00	317,25	253,80
HSLM-A9 (D=26 m)	1319,76	659,88	439,92	329,94	263,95
HSLM-A10 (D=27 m)	1370,52	685,26	456,84	342,63	274,10

Table 4.4: HSLM-A's resonant speeds

Some of the calculated speeds were not considered as they fall outside the range of speeds being studied. It is important to note that all speeds were calculated for the first vertical mode of vibration, as this mode has the most significant impact on the structure's dynamic response compared to higher modes. Since this study's goal is focused on the most adverse conditions, it prioritizes the most critical resonant speeds, which will occur at speeds corresponding to the first vertical mode of vibration. The chosen speeds are depicted in Table 4.5. It is importnat to note that for the HSLM-A7, the resonant speed that generated the most significant impact was 406.08 km/h, leading to bridge vibrations of up to 1g. However, the analysis was based on curves developed for acceleration amplitudes of 0.4g and 0.8g. Since the highest amplitude used to build the Accumulated Track Displacement Curves is 0.8g, any acceleration above this value falls outside the range of the available. Additionally, at amplitudes greater than 0.8g, the ballast becomes so

destabilized that even a single cycle can cause significant instability. As a result, the speed of 406 km/h was excluded from further consideration.

Trains	Speeds in km/h
HSLM-A1	304.00
HSLM-A2	241.11
HSLM-A3	253.80
HSLM-A4	266.00
HSLM-A5	372.24
HSLM-A6	389.16
HSLM-A7	304.56
HSLM-A8	253.80
HSLM-A9	263.92
HSLM-A10	274.10

Table 4.5: tb: HSLM-A chosen speeds

4.3.3 Analysis of Dynamic Responses

For the dynamic analysis of the HSLM-A trains, the speeds illustrated in Table 4.5 were selected based on their impact on amplifying the bridge's dynamic response. It was observed, that the highest speeds did not always correspond to the greatest amplification. Therefore, the chosen speeds were those that led to the highest acceleration amplitudes, ensuring an evaluation of the bridge's behavior under the most critical resonant conditions.

The results of the acceleration-time histories at the midspan of the bridge, obtained with the chosen resonant speeds, are illustrated in Figure 4.4.

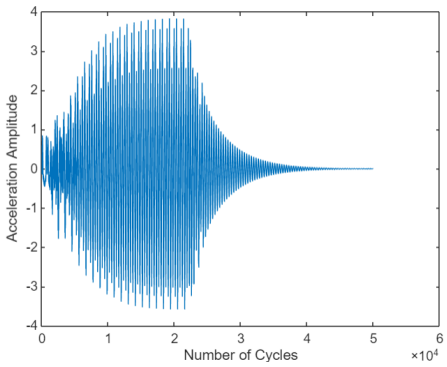

a) HSLM-A1

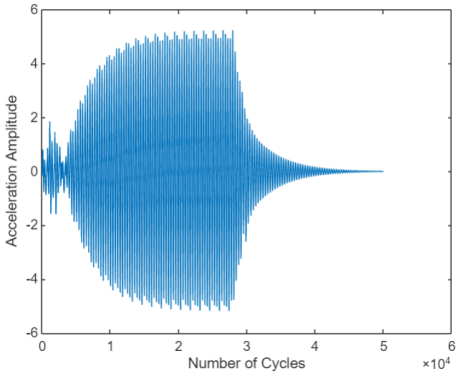

b) HSLM-A2

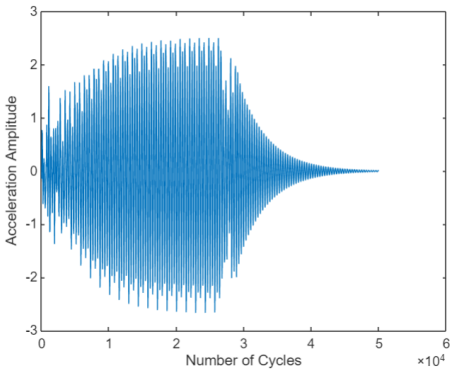

c) HSLM-A3

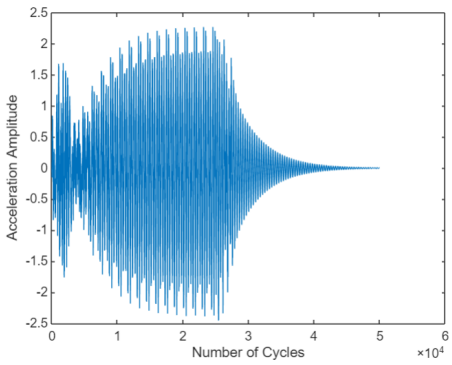

d) HSLM-A4

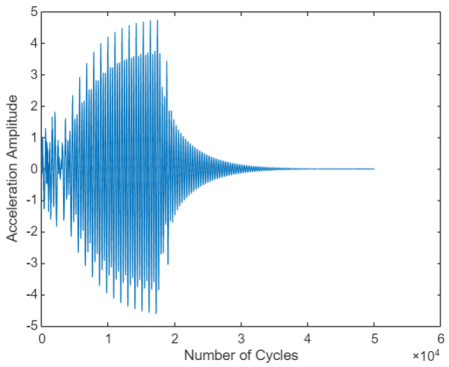

e) HSLM-A5

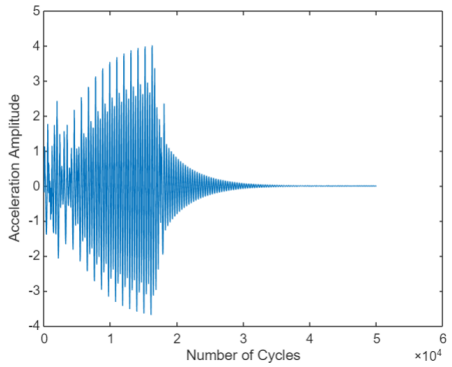

f) HSLM-A6

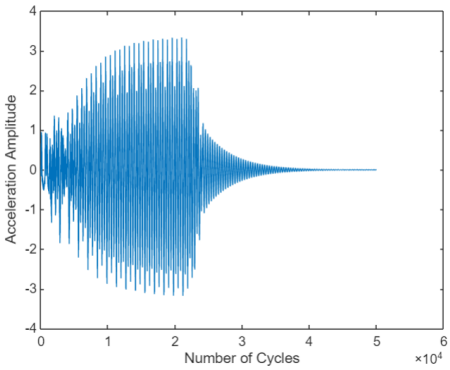

g) HSLM-A7

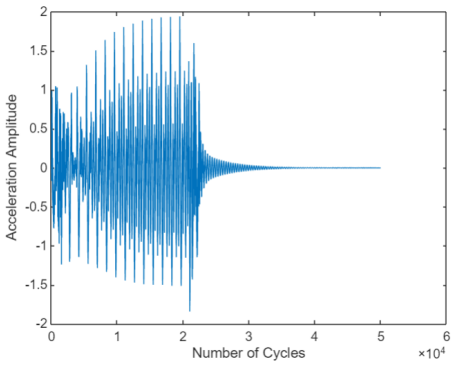

h) HSLM-A8

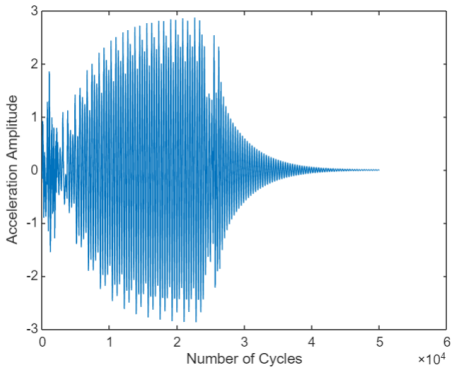

i) HSLM-A9

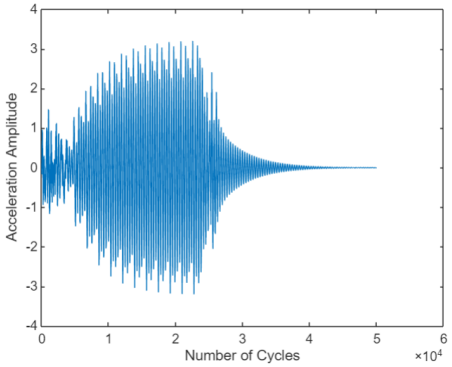

j) HSLM-A10

Figure 4.4: Acceleration-Time histories of all HSLM-A load models

By analyzing the graphs it is clearly noted that resonance occurs. This is indicated by the peaks in the acceleration-time histories at specific frequencies, which match the bridge natural frequency. At these resonant frequencies the system absorbs effectively the energy from the train, causing the bridge to vibrate with substantially higher amplitudes compared to other frequencies.

The rainflow counting method was then utilized to examine the acceleration-time histories obtained from all HSLM-A dynamic simulations. By applying this cycle counting method it was possible assess the number of cycles the bridge experienced, with each cycle being associated to a certain acceleration amplitude value. Thus, through this counting process a acceleration-time spectrum is produced and typically depicted as a form of a histogram. Only one histogram is shown here as a representative example, as illustrated in Figure 4.5.

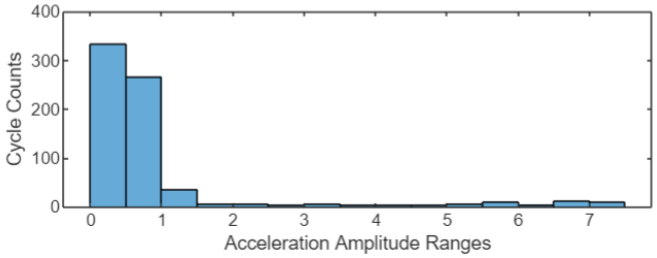

Figure 4.5: Acceleration-time spectrum for the HSLM-A1

The histogram represents the acceleration amplitude ranges, and in this case study, the maximum absolute values of the acceleration amplitudes are used, which are half of these ranges. For instance, a acceleration cycle counted between -4 m/s^2 and 4 m/s^2 results in an amplitude range of 8 m/s^2, while the maximum amplitude is 4 m/s^2. This approach aligns with the use of maximum absolute acceleration values as done in the past experiences performed by Baeßler (2008), described in section 3.3..

The Spectrum was then applied to all three modified Accumulated Track Displacement Curves, linear-linear, linear-logarithmic and logarithmic-logarithmic developed in Section 3.3. By correlating the acceleration ranges, identified in the spectrum with the fatigue strength of the ballast, as indicated by the Accumulated Track Displacement Curve, it was possible to estimate the accumulated damage for a single passage at the resonant speed. Using the Palmgren-Miner Rule, calculations were conducted to assess the damage caused by the single passages of each HSLM-A train. The cumulative damage from the passages of each HSLM-A train is presented in Table 4.6 for each of the three different Accumulated Track Displacement Curves: linear-linear scale, linear-logarithmic scale, and logarithmic-logarithmic scale.

The accumulated damage represents represents the amount of displacement approaching the 1mm lateral displacement failure with each train passage. Taking the 0.5066 damage value as an example, an accumulated damage value of 0.5 means that one train passage causes 50% of the total 1mm lateral displacement that would lead to failure. In other words, after two passages, the full 1mm displacement would be reached, leading to failure. Lower accumulated damage values indicate that more train passages are needed to reach failure.

Trains	Accumulated damage		
	lin-lin scale	lin-log scale	log-log scale
HSLM-A1	0,5066	0,0457	0,0189
HSLM-A2	0,3543	0,2183	0,2783
HSLM-A3	0,3495	0,0223	0,0025
HSLM-A4	0,5408	0,0267	0,0013
HSLM-A5	0,246	0,0468	0,035
HSLM-A6	0,2496	0,0224	0,0094
HSLM-A7	0,4881	0,0326	0,0073
HSLM-A8	0,4415	0,0157	8,42E-05
HSLM-A9	0,2897	0,0214	0,0036
HSLM-A10	0,3414	0,0258	0,0061

Table 4.6: Damage values for all HSLM-A trains

4.4 Evaluation on the Ballast Lateral Stability

4.4.1 Influence of the cut-off values from the Accumulated Track Displacement Curve in the track damage

This process summarized in Figure 3.19 was repeated for for all HSLM-A trains to calculate the damage caused by each single train passage. The primary objective was to assess the influence low amplitude cycles had on the ballast bedding damage, so a damage evaluation was conducted using four different cut-off values: 0.1g, 0.2g, 0.3g, and 0.4g for all Accumulated Track Displacement Curves. Selecting an appropriate cut-off value is particularly challenging due to the limited available data. Each HSLM-A train model (from A1 to A10) responds similarly to the different cut-off values, however the damage values for each Accumulated Track Displacement Curve differ significantly. Figure 4.6 presents the linear-linear Accumulated Track Displacement Curve for both HSLM-A3 and HSLM-A8 load models. As depicted in Figure 4.6 a), for the HSLM-A3, an acceleration amplitude cut-off value of 0.3g shows almost no damage. This is expected because for high cut-off values, we exclude a significant number of cycles with lower amplitudes. Consequently, high cut-offs such as 0.3g and 0.4g are not particularly realistic or useful for practical assessments, as they neglect the cycles with lower amplitudes. Instead, it is the low cut-off values that are crucial to explore. These lower values are essential for evaluating the damage a material can endure over an infinite number of cycles, similar to the high-cycle zone depicted in the original S-N curves of fatigue analysis. By focusing on these lower cut-off values, we can better understand and assess the long-term effects and durability of the ballast under continuous low-amplitude stress.

These cut-offs are designed to evaluate damage from low-amplitude cycles, and Figure 4.6 illustrates that even a small cut-off value, such as 0.1g, significantly reduces the estimated damage for both HSLM-A3 and HSLM-A8 models. This indicates that small changes in the cut-off value

can lead to substantial variations in the damage prediction. In fact, for almost every model, a lower cut-off value substantially affects the damage assessment, highlighting that small amplitude cycles can have a significant impact on the overall accumulated damage.

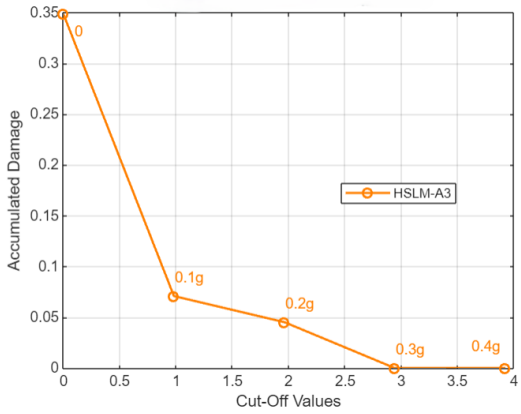

a) HSLM-A3

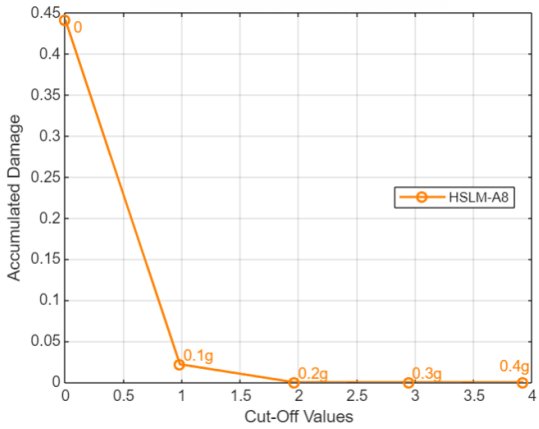

b) HSLM-A8

Figure 4.6: HSLM-A3 and HSLM-8 damage for different cut-off values

Analyzing both accumulated track displacement curves, it becomes evident that the damage without any cut-off value is significantly higher than when using a low cut-off value, such as 0.1g. For example, in the HSLM-A8 model (Figure 4.6 b)), the damage decreases to about 5% when a 0.1g cut-off is applied, compared to the damage observed without any cut-off. This substantial decrease highlights the significant impact that low-amplitude cycles have on ballast damage during single train passages.

The impact of these low-amplitude cycles is crucial, as they accumulate over numerous cycles and play a significant role in ballast instability. Given the importance of these low-amplitude cycles, it is essential to further study the Accumulated Track Displacement Curve for these low amplitudes. Currently, the curve is still quite conservative due to limited experimental data. Future research is needed to better understand how low-amplitude cycles from single train passages contribute to vibration-induced creep.

4.4.2 Influence of the type of the formulation of the Accumulated Track Displacement Curves in the track damage results

In this analysis, the impact of various cut-off values on all three types of accumulated track displacement curves—linear-linear, linear-logarithmic, and logarithmic-logarithmic—was evaluated. Each type of curve reacts uniquely to the cut-off values. As mentioned, the different scales used in the curves can significantly affect the resulting values. Switching from a linear to a logarithmic scale on the x-axis extends the range from thousands to millions of cycles, making the resulting values more conservative and not very reliable.

For example, by examining all the curves of the HSLM-A3 (Figure 4.7), the differences between the three graphs can be highlighted. By examining the three graphs it is clear that logarithmic-logarithmic curve significantly differs from the other two. For the log-log curve, the damage remains almost unchanged across all cut-off values (Figure 4.7 c)). To further illustrate this, additional cut-off values were presented on the log-log graph, making it clearer that damage remains consistent regardless of the cut-off values. This occurs because the log-log scale stretches the cycle count to millions, and the incremental damage for such an extensive number of cycles is minimal and nearly negligible. Only when higher cut-off values are applied do we observe any significant change in the damage on the log-log curve.

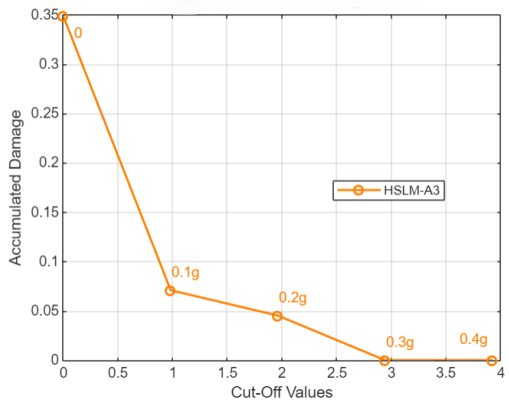

a) HSLM-A3 linear-linear scale

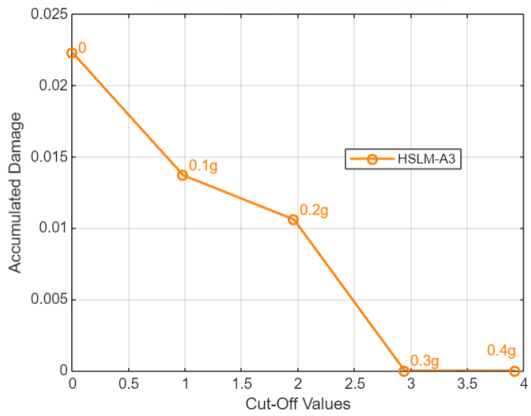

b) HSLM-A3 linear-logarithi«mic scale

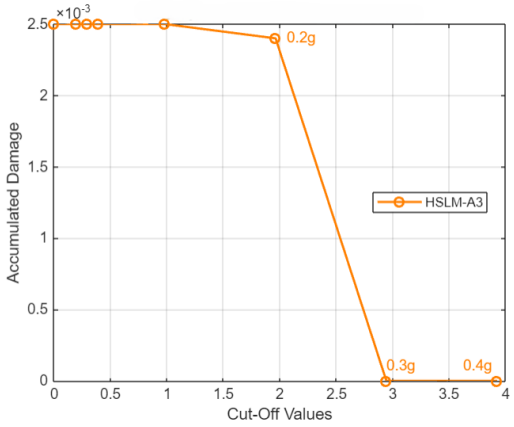

a) HSLM-A3 logarithmic-logarithmic scale

Figure 4.7: Accumulated Track Displacement Curves for the HSLM-A3

When comparing the linear-linear (lin-lin) and linear-logarithmic (lin-log) curves, it is clear that they are quite similar, with only minor differences. Both types of curves reveal that low-amplitude cycles have the most significant impact on damage. In the linear-logarithmic (lin-log) graph, the difference in damage between a scenario with no cut-off value and one with a low cut-off value is less significant compared to the linear-linear (lin-lin) curve. However, even in the lin-log curve, it is evident that low-amplitude cycles still contribute significantly to damage.

To further investigate the impact of cut-off values, the same set of linear-linear (lin-lin), linear-logarithmic (lin-log), and logarithmic-logarithmic (log-log) curves were plotted for the HSLM-A8 load model, as depicted in Figure 4.8.

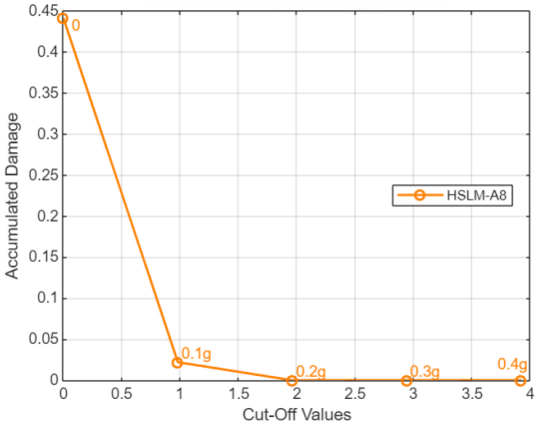

a) HSLM-A8 linear-linear scale

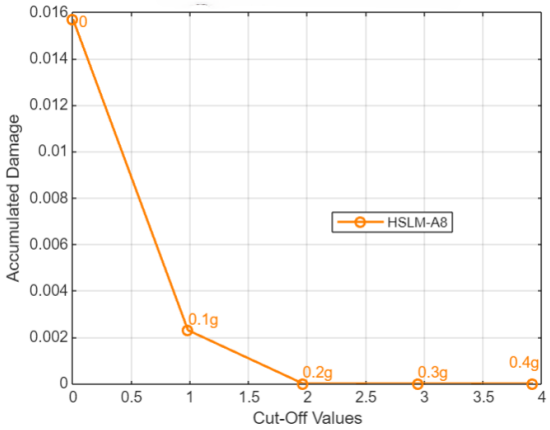

b) HSLM-A8 linear-logarithimic scale

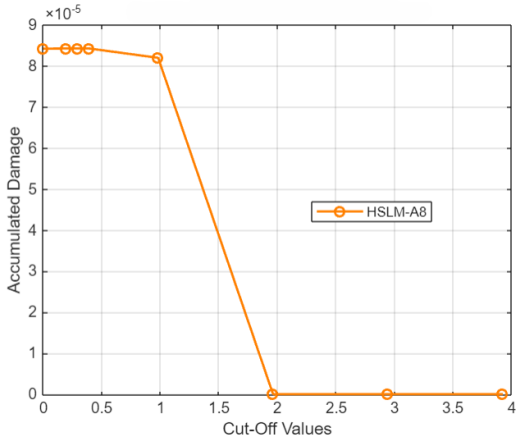

c) HSLM-A8 logarithmic-logarithmic scale

Figure 4.8: Accumulated Track Displacement Curves for the HSLM-A8

The log-log graph, depicted with additional cut-off points for better clarity (Figure 4.8 c)) consistently demonstrates similar behavior. Like the results for the HSLM-A3, the log-log curve once again does not provide conclusive results, as the damage remains unchanged across the different cut-off values. This scenario occurs consistently across all HSLM-A train models, making the log-log approach not very reliable and realistic. Therefore, no definitive conclusions can be drawn from the logarithmic-logarithmic Accumulated Track Displacement Curve.

The comparison between the lin-lin and lin-log graphs (Figure 4.8 a) and Figure 4.8 b) respectively) demonstrates great repeatability with the HSLM-A3 load model. Once more the results indicate that the curves are similar to each other, with low-amplitude cycles showing a significant impact on the damage. However, when examining the damage values from each curve, significant differences emerge. The damage values in the lin-log accumulated track displacement curve are much smaller than those in the lin-lin curve. This discrepancy arises because the lin-lin curve focuses more on the smaller amplitude cycles. In the lin-log curve, the x-axis is on a logarithmic scale, which extends the number of cycles to a much larger range compared to the lin-lin curve.

Figure 4.9 is presented to clarify the analysis. Examining Figure 4.9 with all three Accumulated Track Displacement Curves reveals that for an acceleration amplitude of 2 m/s^2, the number of cycles in the lin-lin curve is much smaller than in the lin-log curve. Specifically, the lin-lin curve shows 1135 cycles, whereas the lin-log curve shows 5931 cycles, for an amplitude of 2 m/s^2. According to the Palmgren-Miner damage accumulation formula (Eq. 3.29), a higher number of cycles results in significantly lower damage, as the formula divides the number of applied cycles by the number of cycles that would lead to failure. Consequently, the lin-log curve produces much smaller damage values, making the lin-lin curve more conservative due to its higher damage values. As mentioned before, past BAM experiments have indicated the lin-log approach to be more effective in assessing the impact of acceleration amplitudes on ballast stability. However, to achieve a more comprehensive understanding of how low-amplitude cycles impact ballast instability, further numerical modeling is needed.

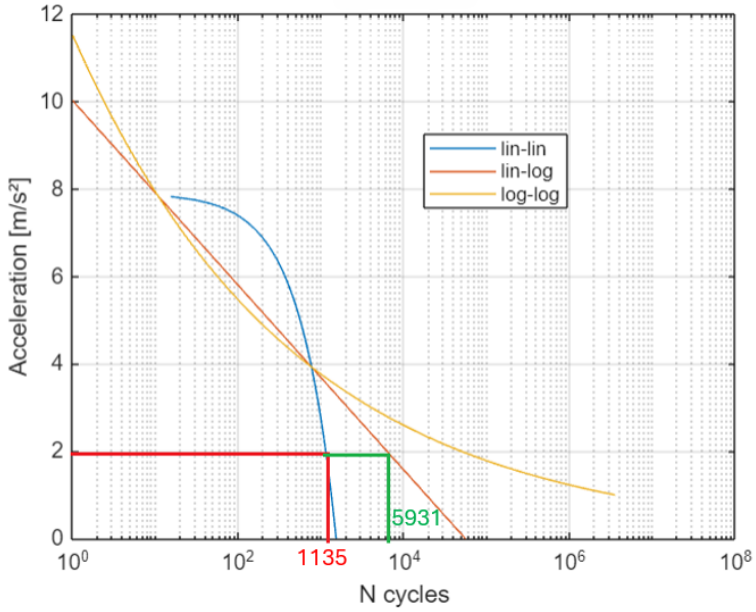

Figure 4.9: Comparison of cycle counts and damage across all three curves for 2 m/s^2

In addition to the primary focus, the research also addresses the calculated damage caused from each single train passage and measures the corresponding maximum bridge deck acceleration amplitudes. By conducting this analysis it allows us to assess whether the maximum acceleration, as stipulated by the EN 1990 Annex (2001), is indeed the most critical factor. With the data from various train passages we obtain a much comprehensive understanding of the dynamic responses and their associated impact on the ballast lateral stability.

By analyzing Table 4.7 it is noted that the highest acceleration values do not always correspond to the highest damage values. Even though the bridge acceleration for the HSLM-A6 is nearly twice that of the HSLM-A4, the damage is lower. To investigate this exception further, a detailed analysis of these specific cases was conducted to identify, which factors are contributing to this unexpected relationship. It is important to note that the acceleration values presented in

Trains	a_{max} $[m/s^2]$	damage	Damage with the "Cut-off" value			
			0,1g	0,2g	0,3g	0,4g
HSLM-A1	3,83	0,0457	0,030	0,0285	0,0211	7,115E-08
HSLM-A2	5,24	0,2183	0,211	0,2099	0,2082	0,1994
HSLM-A3	2,50	0,0223	0,0137	0,0106	4,99E-08	4,99E-08
HSLM-A4	2,27	0,0267	0,010	0,0048	7,785E-08	7,785E-08
HSLM-A5	4,74	0,0468	0,0411	0,0397	0,0369	1,97E-02
HSLM-A6	4,01	0,0229	0,0166	0,0149	0,0093	3,53E-08
HSLM-A7	3,33	0,0326	0,0175	0,16	0,008	6,96E-08
HSLM-A8	1,94	0,0157	0,0023	6,54E-08	6,54E-08	6,54E-08
HSLM-A9	2,87	0,0214	0,0139	0,0116	4,075E-08	4,075E-08
HSLM-A10	3,20	0,0258	0,0167	0,0199	0,0052	4,84E-08

Table 4.7: Damage of single train passages for the linear-logarithmic scale

the table are the maximum absolute values. The detailed analysis revisits the histograms that display amplitude ranges, which are twice the maximum absolute acceleration values, as previously explained.

When analyzing the histograms of HSLM-A acceleration profiles (see Figure 4.10), an interesting observation stands out: despite HSLM-A6 exhibiting significantly higher acceleration amplitude ranges, the number of cycles within these ranges is surprisingly small. In contrast, HSLM-A4, which reaches much lower maximum acceleration range up to 4.8 m/s², shows a substantially higher frequency of cycles across its acceleration spectrum. For instance, within the acceleration range of 0 to 5 m/s², HSLM-A6 registers only 331 cycles, whereas HSLM-A4 records 747 cycles, more than double despite its lower peak values. This discrepancy is in accordance with fatigue analysis principles: the number of cycles, rather than just the peak values, plays a crucial role in determining damage accumulation. HSLM-A4, with its more frequent and varied acceleration cycles, contributes more significantly to cumulative damage compared to HSLM-A6's high peaks.

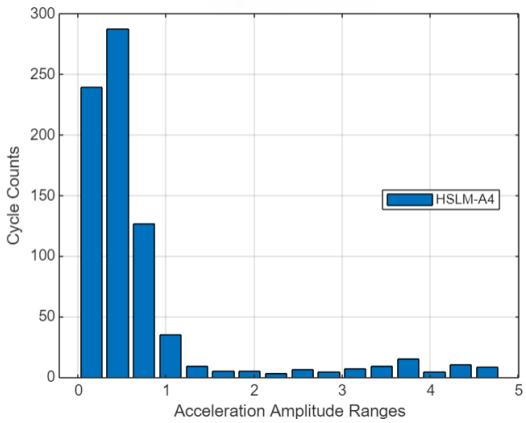

a) HSLM-A4

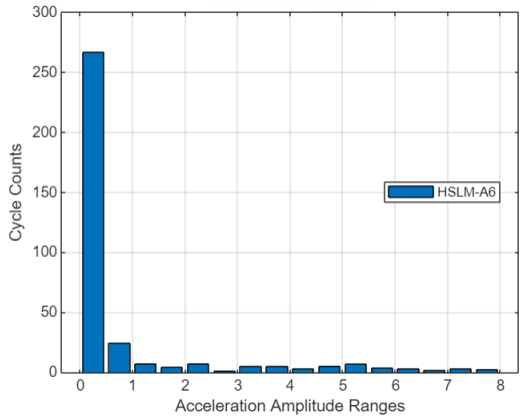

b) HSLM-A6

Figure 4.10: HSLM-A4 and HSLM-A histograms

This pattern is observed not only in HSLM-A6 and HSLM-A4 but also in other HSLM-A models such as A3, A9, and A10. Once again, the data reveal that smaller acceleration cycles are more influential in contributing to cumulative damage than the high amplitude peaks.

This analysis clearly indicates that the maximum acceleration does not always correlate with the highest damage to the ballast. This observation highlights that depending solely on maximum acceleration, as specified by the EN-1990 Annex A2 criterion, may be inadequate for a comprehensive damage assessment. Currently, the EN-1990 Annex A2 criterion relies exclusively on maximum acceleration, which may overlook the effects of varying amplitude cycles on ballast stability. Therefore, it is recommended to adopt a new approach that incorporates the number of cycles into the analysis.

Chapter 5

Conclusions and Future Work

5.1 Conclusions

The primary objective of this dissertation was to evaluate the operational safety of high-speed trains on ballasted track bridges through a dynamic analysis of bridge-train interaction. This involved calculating the accumulated damage from each singular passage of all HSLM-A load models and the corresponding maximum acceleration at mid-span of the bridge, in relation to the maximum acceleration limit stipulated in EN 1992-2. The study focused on simulating the passage of high-speed trains over bridges using the HSLM-A load models at resonant speeds ranging from 140 km/h to 420 km/h.

Using a combination of MATLAB coding and ANSYS modeling, input parameters based on mechanical and geometric properties were defined for each case study. Each simulation represented a train crossing a specific bridge, producing the time history of vertical accelerations at mid-span, which is critical for safety verification. Additionally, a key aspect of this study was the analogy to fatigue analysis, particularly using rainflow counting and the calculation of accumulated damage in the ballast layer. This approach allowed for a detailed examination of how single train passages impact the ballast layer, similar to fatigue in materials subjected to cyclic loading. Various aspects were explored, such as various HSLM-A train models, along with different cut-off values to better understand their influence on the damage accumulation.

This dissertation highlighted the complexities involved in analyzing the phenomenon of vibration-induced creep. To explore this, the concept of cut-off values for acceleration amplitudes was employed, revealing critical insights into how different cut-off values affect damage assessment for single train passages. Specifically, it was found that low cut-off values (e.g., 0.1g) have a significant impact on the evaluation of ballast damage compared to higher cut-offs. The introduction of low cut-off values showed that small amplitude cycles play a crucial role in understanding cumulative damage over many cycles. By setting a lower cut-off value, the analysis was able to capture a larger number of low amplitude cycles, which are often neglected in assessments using higher cut-offs. These low amplitude cycles, despite their smaller individual impact, accumulate significant damage over time due to their high frequency. This underscores the importance of including

low amplitude cycles in damage assessments to gain a comprehensive understanding of the track's long-term stability.

Additionally, the type of formulation used for the accumulated track displacement curves—linear-linear (lin-lin) versus linear-logarithmic (lin-log)—also influenced the damage assessment outcomes. The lin-log curve, which extends the x-axis logarithmically, places greater emphasis on low amplitude cycles by representing a larger range of cycle counts. This approach aligns with previous BAM experiments, which found the lin-log method more effective in assessing the impact of different acceleration amplitudes on ballast stability. However, the lin-log formulation results in lower damage values compared to the lin-lin formulation due to the higher number of cycles it considers, making it less conservative but potentially more accurate for long-term predictions.

Furthermore, contrary to the stipulations of the EN-1990 Annex A2, the study demonstrated that the crucial factor is not always the maximum acceleration of the bridge deck but rather the number of cycles with varying amplitudes to which the ballast layer is subjected. The maximum acceleration did not consistently correspond to the highest damage; in some HSLM-A load models, the accumulated damage was greater for lower maximum acceleration values due to the higher number of cycles with smaller amplitudes.

Therefore, it is recommended to approach vibration-induced creep through the number of cycles, similar to fatigue analysis, rather than considering the maximum acceleration as the principal factor. This dissertation underscores the need for a more comprehensive evaluation of ballast layer damage, taking into account the cumulative effects of varying amplitude cycles to ensure the lateral track stability and lower the risk of derailment.

5.2 Future Work

The course of this research raise several questions that were not addressed. In this context, some topics requiring further analysis are referred in the following paragraphs:

- **Limitations of Case Study Approach:** This study only included a case study, which limits the ability to validate and generalize the conclusions across different scenarios. The findings are specific to the particular lateral track model and parameters used, which significantly limits the results. For instance, the study was conducted for a specific temperature variation, as a basis for the Accumulated Track Displacement Curves. A change in temperature would influence the compression forces N_T, and as a result, the Accumulated Track Displacement Curves would change.

- **Developing a Realistic Accumulated Track Displacement Curve:** To achieve a more realistic Accumulated Track Stability Curve, a significantly larger number of analyses is required. Especially for low amplitudes, which have been shown to have a greater impact on ballast instability. Conducting extensive tests and simulations will provide robust data for millions of cycles, enabling a precise determination of track stability under high-speed train operations.

- **Adapting Normative Criteria:** Based on the findings related to the vibration-induced creep phenomenon and its impact on ballast stability, it is recommended to adapt the existing normative criteria. Current standards should consider the number of cycles and varying amplitudes experienced by the ballast layer, rather than solely focusing on maximum acceleration. However, the development of a improved normative criterion requires further investigation. Applying realistic train load collectives is essential to capture the true operational conditions of railway systems. Alternatively, research should explore whether HSLM-A load models can adequately simulate the effects of real trains.

- **Expanding the Range of Bridges and Trains Analyzed:** To validate and generalize the conclusions drawn in this study, it is essential to analyze a bigger range of bridge types and high-speed train models. This will help how dynamic behavior and accumulated damage can change across different structural and operational scenarios.

- **Dynamic Analysis of Continuous Bridges:** Future research should include dynamic analyses of continuous bridges with intermediate piers. Exploring different structural solutions will provide a comprehensive understanding of how bridge continuity and pier configurations affect the dynamic response and safety of high-speed rail operations.

- **Incorporating External Actions:** The influence of additional external actions, such as wind and seismic events, on the operational safety of railway bridges should be investigated. These factors could significantly impact the dynamic behavior of bridges and the stability of ballast, thereby influencing the overall safety criteria.

Bibliography

EN 1993-1-9. Eurocode 3: Design of steel structures-part 1-9: Fatigue. *European Committee for Standardization: Brussels, Belgium*, 2005.

ERRI D 214/RP8. Rail bridges for speeds $>$ 200 km/h: Confirmation of values against experimental data. *Technical report, European Rail Research,Institute, Utrecht*, 1999.

ERRI D 214/RP9. Rail bridges for speeds $>$ 200 km/h. *Final report. Technical report, European,Rail Research Institute, Utrecht*, 1999.

ERRI D 202 / RP 7. Verbesserung der Kenntnis über die Kräfte im lückenlosen Gleis (einschließlich Weichen) – Synthesebericht zu den Messungen des Quer- und Längsverschiebewiderstands, 1999.

Guilherme Alencar, Jeong K Hong, Abilio de Jesus, José Guilherme S da Silva, and Rui Calçada. The master sn curve approach for fatigue assessment of welded bridge structural details. *International Journal of Fatigue*, 152:106432, 2021.

Therese Arvidsson, Andreas Andersson, and Raid Karoumi. Train running safety on non-ballasted bridges. *International Journal of Rail Transportation*, 7(1):1–22, 2019. doi: 10.1080/23248378.2018.1503975.

Matthias Baeßler. Lagever änderungen des schottergleises durch zyklische und dynamische beanspruchungen. *Nao sei*, 2008.

Matthias Baeßler and Dr Werner Rücker. Improved acceptance limits for bridge deck vibrations in light of test results, railway engineering. *Railway Engineering*, 2007.

C. Baptista. *Multiaxial and Variable Amplitude Fatigue in Steel Bridges*. PhD thesis, Ecole Polytechnique Fédérale de Lausanne, 2016. URL https://doi.org/10.5075/EPFL-THESIS-7044.

Anil K Chopra. Dynamics of structures: Theory and applications to earthquake engineering, prentice hall. *Inc., Upper Saddle River, NJ*, 1995.

Ray W. Clough and Joseph Penzien. *Dynamics of Structures*. McGraw-Hill Kogakusha, Tokyo, 1975.

Ray W. Clough and Joseph Penzien. *Dynamics of Structures*. McGraw-Hill, Inc., New York City, NY, USA, 3rd edition, 2003.

Pablo Cuéllar, Matthias Baeßler, and Werner Rücker. Ratcheting convective cells of sand grains around offshore piles under cyclic lateral loads. *Granular Matter*, 11:379–390, 2009.

R Moreno Delgado et al. Modelling of railway bridge-vehicle interaction on high speed tracks. *Computers & Structures*, 63(3):511–523, 1997.

Pedro Aires Moreira Montenegro e Almeida. Comportamento dinâmico de uma ponte em arco existente para tráfego ferroviário de alta velocidade. Master's thesis, Faculdade de Engenharia da Universidade do Porto, 2008.

Coenraad Esveld. Improved knowledge of cwr track. In *Interactive Conference on Cost Effectiveness and Safety Aspects of Railway Track, UIC/ERRI, Paris*, pages 8–9, 1998.

European Commission. Commission regulation (eu) no 1299/2014 of 18 november 2014 on the technical specifications for interoperability relating to the 'infrastructure' subsystem of the rail system in the european union text with eea relevance, December 2014.

European Commission. The european green deal. Report to the European Parliament, European Council, European Economic and Social Committee, and Committee of the Regions, 2019.

European Parliament and Council of the European Union. Decision (eu) 2020/2228 of the european parliament and of the council of 23 december 2020 on a european year of rail (2021), December 2020.

Federal Railroad Administration (FRA). The influence of track maintenance on the lateral resistance of concrete tie track, 2003.

L. Frýba. *Dynamics of Railway Bridges*. Thomas Telford, Prague, 1996.

José M Goicolea and Felipe Gabaldón. Dynamics of high-speed railway bridges: Methods and design issues. *Bridge Vibration and Controls: New Research*, pages 89–111, 2012.

Heinrich Hertz. Ueber die berührung fester elastischer körper. 1882.

International Union of Railways. *Title of the Book or Document*. Publisher Name, Publisher Location, 2018. Any additional note if needed.

JJ0414 Kalker. The computation of three-dimensional rolling contact with dry friction. *International Journal for numerical methods in engineering*, 14(9):1293–1307, 1979.

Andrew Kish, Gopal Samavedam, et al. Track buckling prevention: theory, safety concepts, and applications. Technical report, John A. Volpe National Transportation Systems Center (US), 2013.

Mirko Klesnil and P Lukác. *Fatigue of metallic materials*, volume 71. Elsevier, 1992a.

Mirko Klesnil and P Lukác. *Fatigue of metallic materials*, volume 71. Elsevier, 1992b.

Xiaoyan Lei and N-A Noda. Analyses of dynamic response of vehicle and track coupling system with random irregularity of track vertical profile. *Journal of sound and vibration*, 258(1):147–165, 2002.

W. Rücker M. Baeßler, P. Cuéllar. The lateral stability of ballasted tracks on vibrating bridge decks. *International Journal of Railway Technology*, 2014.

P. Montenegro. *A methodology for the assessment of the train running safety on bridges*. Phd thesis, Faculdade de Engenharia da Universidade do Porto (FEUP), Porto, Portugal, 2015.

P. A. Montenegro, H. Carvalho, D. Ribeiro, R. Calçada, M. Tokunaga, M. Tanabe, and W. M. Zhai. Assessment of train running safety on bridges: A literature review. *Engineering Structures*, 2021.

SGM Neves, AFM Azevedo, and R Calçada. A direct method for analyzing the vertical vehicle–structure interaction. *Engineering Structures*, 34:414–420, 2012.

N Nikitas, JHG Macdonald, and KD Tsavdaridis. Modal analysis. *Encycl. Earthq. Eng*, 23:1–22, 2014.

João Pombo, Jorge Ambrósio, and Miguel Silva. A new wheel–rail contact model for railway dynamics. *Vehicle System Dynamics*, 45(2):165–189, 2007.

Diogo Rodrigo Ferreira Ribeiro et al. Comportamento dinâmico de pontes sob acção de tráfego ferroviário a alta velocidade. *nao sei*, 2004.

Ahmed A Shabana, Khaled E Zaazaa, José L Escalona, and Jalil R Sany. Development of elastic force model for wheel/rail contact problems. *Journal of sound and vibration*, 269(1-2):295–325, 2004.

Ahmed A Shabana, Khaled E Zaazaa, and Hiroyuki Sugiyama. *Railroad vehicle dynamics: a computational approach*. CRC press, 2007.

R. Sharpe and R Bentley. Dynamics of structures by ray w. clough and joseph penzien. mcgraw-hill 1975. 634 pp. illus. *Bulletin of the New Zealand Society for Earthquake Engineering*, 1977.

H. Sugiyama, K. Araki, and Y. Suda. On-line and off-line wheel/rail contact algorithm in the analysis of multibody railroad vehicle systems. *Journal of Mechanical Science and Technology*, 2009.

Theodore Sussmann, Andrew Kish, and Michael Trosino. Influence of track maintenance on lateral resistance of concrete-tie track. *Transportation research record*, 1825(1):56–63, 2003.

A. Tembe. Fadiga em pontes mistas aço-betão. Master's thesis, Instituto Superior Técnico, Universidade Técnica de Lisboa, Lisboa, 2001.

M.A. Van. *Stability of Continuous Welded Rail Track*. Delft University Press, 1997.

Fuheng Yang and GHISLAIN A FONDER. An iterative solution method for dynamic response of bridge–vehicles systems. *Earthquake engineering & structural dynamics*, 25(2):195–215, 1996.

Manfred Zacher and Matthias Baeßler. Dynamic behaviour of ballast on railway bridges. in dynamics of high–speed railway bridges. selected and revised papers from the advanced course on 'dynamics of high–speed railway bridges', porto, portugal, 20–23 september 2005. *CRC Press*, 2008.